Highlights

1) Mouse models of hearing, acquired loss, and deafness studied at 1, 3, and 6 months.
2) Endbulbs and bushy cells developed normally to 1 month of age.
3) Hearing loss led to subsequent atrophy of endbulbs of Held and bushy cells.
4) The magnitude and cumulative duration of loss resulted in more severe pathologies.

Title

The effect of progressive hearing loss on the morphology of endbulbs of Held and bushy cells

Author Names and Affiliations

Catherine J. Connelly[a,b], David K. Ryugo[a,b,c], and Michael A. Muniak[a]

[a] Hearing Research Unit, Garvan Institute of Medical Research, Sydney, NSW 2010, Australia

[b] School of Medical Sciences, Faculty of Medicine, University of New South Wales, Sydney, NSW 2052, Australia

[c] Department of Otolaryngology, Head, Neck & Skull Base Surgery, St Vincent's Hospital, Sydney, NSW 2010, Australia

Corresponding Author

Catherine J. Connelly

384 Victoria St., Darlinghurst, NSW 2010, Australia

Tel: +61 2 9295 8381

Email: catconnelly22@gmail.com

Abstract

Studies of congenital and early-onset deafness have demonstrated that an absence of peripheral sound-evoked activity in the auditory nerve causes pathological changes in central auditory structures. The aim of this study was to establish whether progressive acquired hearing loss could lead to similar brain changes that would degrade the precision of signal transmission. We used complementary physiologic hearing tests and microscopic techniques to study the combined effect of both magnitude and duration of hearing loss on one of the first auditory synapses in the brain, the endbulb of Held (EB), along with its bushy cell (BC) target in the anteroventral cochlear nucleus. We compared two hearing mouse strains (CBA/Ca and heterozygous *shaker-2*$^{+/-}$) against a model of early-onset progressive hearing loss (DBA/2) and a model of congenital deafness (homozygous *shaker-2*$^{-/-}$), examining each strain at 1, 3, and 6 months of age. Furthermore, we employed a frequency model of the mouse cochlear nucleus to constrain our analyses to regions most likely to exhibit graded changes in hearing function with time. No significant differences in the gross morphology of EB or BC structure were observed in 1-month-old animals, indicating uninterrupted development. However, in animals with hearing loss, both EBs and BCs exhibited a graded reduction in size that paralleled the hearing loss, with the most severe pathology seen in deaf 6-month-old *shaker-2*$^{-/-}$ mice. Ultrastructural pathologies associated with hearing loss were less dramatic: minor changes were observed in terminal size but mitochondrial fraction and postsynaptic densities remained relatively stable. These results indicate that acquired progressive hearing loss can have consequences on auditory brain structure, with prolonged loss leading to greater pathologies. Our findings suggest a role for early intervention with assistive devices in order to mitigate long-term pathology and loss of function.

Highlights

1) Mouse models of hearing, acquired loss, and deafness studied at 1, 3, and 6 months.
2) Endbulbs and bushy cells developed normally to 1 month of age.
3) Hearing loss led to subsequent atrophy of endbulbs of Held and bushy cells.
4) The magnitude and cumulative duration of loss resulted in more severe pathologies.

Keywords

Auditory nerve; Cochlear nucleus; Deafness; Ultrastructure

Abbreviations

ABR, auditory brainstem response; AN, auditory nerve; AVCN, anteroventral cochlear nucleus; BC, bushy cell; CN, cochlear nucleus; DAB, 3,3'-diaminobenzadine; DCN, dorsal cochlear nucleus; EB, endbulb of Held; EGFP, enhanced green fluorescent protein; EM, electron microscopy; G, glutaraldehyde; GFP, green fluorescent protein; GlyT2, glycine transporter 2; P, paraformaldehyde; PSD, postsynaptic density; PVCN, posteroventral cochlear nucleus; RMS, root mean square; SD, standard deviation; SEM, standard error of the mean; *sh2*, *shaker-2*; VCN, ventral cochlear nucleus

1. Introduction

The ability to accurately detect, localize, and perceive sound relies on accurate connectivity, precise timing, and rapid transmission of neural signals throughout the brain. If any part of the auditory pathway is damaged, the result is an impaired perception of the acoustic environment. Sensorineural hearing loss is primarily caused by pathology in the inner ear affecting the sensory receptors or primary auditory neurons. One of the conundrums of hearing loss is the emergence of symptoms such as difficulty hearing sound in noise, loudness distortion, and tinnitus—issues that are not effectively remedied by sound amplification. There is growing evidence that these symptoms are not created in the ear per se but rather by reactive changes within the central nervous system. Indeed, plastic changes are frequently observed in the auditory system as sequelae to deafness (Kral et al., 2001; Ryugo et al., 1997, 1998; Shepherd and Hardie, 2001; Snyder et al., 2000; Tirko and Ryugo, 2012; West and Harrison, 1973). Deafness, however, lies at the far end of the hearing loss spectrum, establishing a worst-case benchmark of changes to auditory pathways resulting from long-term sensory deprivation. It is hypothesized that analogous but less severe brain changes would follow acquired progressive hearing loss.

The auditory nerve (AN) delivers signals from the cochlea to the brain, terminating throughout the cochlear nucleus (CN; Muniak et al., 2016). Thus, the AN is first to experience the consequences of hearing loss due to receptor damage, and any pathologies are likely to reverberate throughout the central auditory system. One particular AN synaptic interface, the endbulb of Held (EB), along with its bushy cell (BC) target in the anteroventral CN (AVCN), has been the subject of extensive studies on deprivation-induced plasticity due to its prominent size and specializations for temporal coding. The EB is a large, complex axosomatic ending created

by type I AN fibers (Ryugo and Spirou, 2009) that contains hundreds of active zones in contact with individual BCs (Nicol and Walmsley, 2002; Ryugo et al., 1996). This synaptic junction is designed to allow the auditory spike stream to be transferred from the EB to the BC at rapid rates and with high fidelity (Babalian et al., 2003; Manis and Marx, 1991; Pfeiffer, 1966).

Changes to auditory activity have been shown to affect EB and BC anatomy. When sound-evoked activity in the AN is completely blocked from birth, BCs become smaller (Lesperance et al., 1995; Pasic and Rubel, 1989; Saada et al., 1996; West and Harrison, 1973), and EBs atrophy, losing their complex arborizations (Limb and Ryugo, 2000; Ryugo et al., 1997, 1998; Wright et al., 2014; Youssoufian et al., 2008). In addition, the postsynaptic densities (PSDs) of EB terminals flatten and hypertrophy in congenitally deaf animals (Gulley et al., 1978; Lee et al., 2003; Ryugo et al., 1997). When some residual sound-evoked activity in the AN remains, as noted in a cohort of hard-of-hearing cats, EB structure takes an intermediate form between the large, complex EBs of normal hearing cats and the smaller, atrophied EBs found in congenitally deaf white cats (Ryugo et al., 1998). This observation suggests that EB integrity may be sensitive to graded variations in sound-evoked activity in the AN.

To characterize the effects of acquired progressive hearing loss on EB and BC structure, we utilized the DBA/2 mouse, a strain that exhibits early-onset sensorineural hearing loss. DBA/2 mice begin to display high-frequency hearing loss at 3-4 weeks of age, shortly after hearing onset (P11; Ehret, 1976) and just before sexual maturity (6-7 wks; Green and Witham, 1991); this loss progresses into adulthood to include the remaining mid-to-low frequencies (Henry and Haythorn, 1975; Hultcrantz and Spangberg, 1997; Johnson et al., 2000; Shin et al., 2010; Willott and Erway, 1998; Willott et al., 1984; Zheng et al., 1999). The pattern of hearing loss of the DBA/2 is closely paired to a progressive loss of inner and outer hair cells (Hultcrantz

and Spangberg, 1997), and has been attributed to mutations in two separate proteins—cadherin-23 (Noben-Trauth et al., 2003) and fascin-2 (Shin et al., 2010)—associated with stereocilia stability and function. Changes in synaptic transmission have been observed at the EB-BC interface in older DBA/2 mice (Wang and Manis, 2005, 2006), suggesting structural alterations may be present. Use of this mouse allows us to isolate the effects of auditory threshold loss from the potential confound of senescence in studies of "age-related" hearing loss (Frisina and Walton, 2006), as the loss occurs at a relatively young age.

DBA/2 mice were examined at different age-points corresponding to different stages of progressive hearing loss. This approach was adopted in order to build a comprehensive profile of how EB and BC structure changes with varying degrees and durations of hearing loss. For normal hearing controls, we utilized age-matched CBA/Ca mice (Zheng et al., 1999). We also included congenitally deaf homozygous recessive *shaker-2* (*sh2*$^{-/-}$) mice (Lee et al., 2003; Limb and Ryugo, 2000; Probst et al., 1998), as well as their strain-matched hearing heterozygous *sh2*$^{+/-}$ counterparts to examine the influence of complete sound deprivation. Deafness in *sh2*$^{-/-}$ mice is caused by a mutation in myosin-15, another protein implicated in stereocilia and hair cell function (Liang et al., 1999; Probst et al., 1998).

We identified the frequency range that exhibited the greatest change in hearing thresholds with age in our mouse cohorts—the progression of hearing loss in the DBA/2 mouse is highly variable with frequency (Zheng et al., 1999)—and used a frequency model of the mouse CN (Muniak et al., 2013) to constrain our light and electron microscopic (EM) analyses of each mouse to the corresponding sub-region of its CN. We hypothesized that mice with a greater degree and longer duration of hearing loss would exhibit EB and BC morphology that more closely resembled that of congenitally deaf animals.

2. Methods

2.1 Animals

A total of 56 mice of either sex with CBA/Ca, DBA/2, and *shaker-2* backgrounds were used for this study (Tables 1-3). Mice were grouped into 1-, 3-, and 6-month-old cohorts. Subsets of these mice were transgenic animals expressing enhanced green fluorescent protein (EGFP) under the control of the glycine transporter 2 (GlyT2) gene promoter (Zeilhofer et al., 2005), and were used for EM analysis (GlyT2-EGFP mice; Table 3). Parent GlyT2-EGFP mice with a C57Bl/6 background were obtained from Prof. H.U. Zeilhofer (University of Zurich, Switzerland). CBA/Ca transgenic mice (CBGlyT2-EGFP), $sh2^{+/-}$ transgenic mice ($sh2^{+/-}$GlyT2-EGFP), and $sh2^{-/-}$ transgenic mice ($sh2^{-/-}$GlyT2-EGFP) were obtained by backcrossing the transgene into our mouse strains of interest for at least 10 generations. Genotyping of *sh2* and GlyT2-EGFP mice was completed in-house by the Garvan Molecular Genetics Department to verify hetero- and homozygosity as well as the presence of the transgene. To avoid possible ectopic expression of EGFP, only transgenic heterozygotes were used for analysis (Zeilhofer et al., 2005). Animals were housed in individually ventilated cages with ad libitum access to food and water. All procedures were performed in accordance with NHMRC guidelines and approved by the Animal Ethics Committee of the Garvan Institute of Medical Research and St. Vincent's Hospital, UNSW Australia.

2.2 Auditory Brainstem Response

All mice were subjected to auditory brainstem response (ABR) testing before use. Mice were anesthetized with 100 mg/kg ketamine and 20 mg/kg xylazine in sterile saline and placed

on a small infrared heating pad inside a sound-attenuating chamber (Sonora Technology Co., Gotenba, Japan). Ophthalmic ointment was used to cover the eyes to prevent corneal drying. The right pinna was directed to face a free-field speaker (MF1; Tucker Davis Technologies [TDT], Alachua, FL) placed 10 cm away level with the head. Differential recordings were made using subdermal platinum needle electrodes placed over the vertex of the skull (active), the right bulla (reference), and leg muscle (ground). Broadband clicks (0.1 ms pulse) and tone pips (5 ms duration, 0.5 ms rise/fall) with alternating polarity were generated using a software-controlled signal processor (10/s rate; RZ6/BioSigRZ; TDT). Responses were amplified (RA16PA/RA4LI; TDT), bandpass filtered from 30-3,000 Hz with a 50 Hz notch filter, and averaged over 512 repetitions (RZ6; TDT). Evoked neural activity to clicks and 4-, 8-, 16-, 24-, 32-, and 40-kHz tones were measured at sound levels from 90 to 0 dB SPL in 10 dB steps. ABRs were saved for offline analysis with OpenABR (http://ryugolab.openabr.org/, Samuel Kirkpatrick) an automated auditory threshold detection program. Hearing threshold was defined as the sound level at which the peak ABR amplitude was four times the standard deviation of the average baseline noise level (Bogaerts et al., 2009). If no evoked response was present at the loudest stimulus intensity tested for a click or tone, a nominal threshold value of 110 dB SPL was assigned.

2.3 Auditory Nerve Injection

Nine CBA/Ca, 7 DBA/2, 7 *sh2*$^{+/-}$, and 9 *sh2*$^{-/-}$ mice were used for anterograde tracer dye injections into the auditory nerve to label EB terminals in the CN (Table 2). Mice were prepared for injection using aseptic techniques. Anesthesia was induced using isoflurane (5% in 0.5 L/mm O_2) and maintained (1.5-2%) for the duration of the surgery. Each mouse was visually monitored for respiration rate, and checked for an eye and paw reflex prior to incision and throughout the

procedure. If a reflex was present, the isoflurane dosage was slightly increased until the animal was areflexic and respiration remained steady. Ophthalmic ointment was used to cover the eyes to prevent corneal drying. The auditory nerve injection method was modified from a previously reported method (Limb and Ryugo, 2000). The anesthetized mouse was secured in a nose cone with a bite bar so that the animal lay on its left side with the right ear oriented upward. After removal of hair behind the right ear, 1-2 drops of bupivicaine (5 mg/mL) were topically administered, and a postauricular incision was made. The cartilage comprising the external auditory canal was followed to its connection with the boney opening in the bulla. An incision was then made in the ear canal to expose and excise the tympanic membrane, followed by removal of the malleus and incus. Toothed forceps were used to carefully chip away the caudal and ventral aspects of the bulla to reveal the stapedial artery coursing through the arch of the stapes. For removal of the stapes, the superior and inferior portion of the stapedial artery (with respect to the stapes) was cauterized with a low-temperature, fine-tip cautery (Medtronic, North Ryde, NSW, AUS). After the stapes was extracted, a small hooked probe was inserted into the opening of the oval window to slowly chip off the bone of the otic capsule. Any remaining membranous tissues of the organ of Corti were removed to expose the modilous. An acupuncture needle was then used to gently poke 2-3 holes into the apical and middle-basal regions of the thin modiolar bone, allowing access to the spiral ganglion. Excess fluid from the cochlea was wicked away to prevent it from diluting or washing away the tracer dye during injection. A quartz micropipette with an inner diameter of 80-90 µm filled with 5% Neurobiotin (SP-1120; Vector Laboratories, Burlingame, CA) was attached to a pressure injector (Nanoject II; Drummond Scientific Company, Broomall, PA) fastened to a stereotaxic frame (Stoelting, Wood Dale, IL) and manually lowered into the needle holes in the modilous. A total of ~1 µL of dye

was pressure injected into each cochlea. The dye was allowed approximately 5 min to settle before the pipette was withdrawn and the incision sutured closed. Animals were subcutaneously injected with buprenorphine (0.05 mg/kg) and sterile saline (~0.5 mL) during recovery, and allowed to survive for 4-5 hrs to permit tracer diffusion throughout the axons.

2.4 Injection Recovery

Animals were anesthetized with a lethal injection of pentobarbitone (55 mg/kg, I.P.). When the animal was areflexic to a paw pinch, the chest cavity was opened to expose the heart, and the left ventricle injected with 0.02 mL heparinized saline to minimize clotting. The heart was then transcardially perfused through the right ventricle with 2 mL 1% $NaNO_2$ in 0.1M phosphate buffered saline prewash, followed by 60 mL of a 2%/2% glutaraldehyde/paraformaldehyde in 0.1M phosphate buffered saline solution (pH 7.4). Brains were postfixed overnight at 4 ºC in the fixative solution, dissected from the skull, and embedded in gelatin-albumin hardened with glutaraldehyde. Coronal sections were cut at 60 µm with a vibrating microtome (VT1200S; Leica Biosystems, Nussloch, GER) and free-floating sections were collected in 0.12M Tris buffer (TBS) at room temperature. Sections were treated with 1% H_2O_2 in 0.12M TBS for 10 min to remove endogenous peroxidase, and then rinsed in three changes of 0.12M TBS for 5 min each. Next, the tissue was incubated in an avidin-biotin solution (Vectastain Elite ABC Kit, PK-6100; Vector Laboratories) with 0.1% Triton X-100 (Sigma-Aldrich, St. Louis, MO) for 1 hr. Sections were again rinsed in three changes of 0.12M TBS for 5 min each before being developed in a 0.05% 3,3'-diaminobenzadine (DAB), 0.4% nickel ammonium sulfate, and 0.035% H_2O_2 solution in 0.12M TBS to give the tracer dye a dark purple color. The stained free-floating tissue sections were then mounted on gelatin coated

slides, counterstained for Nissl substance with cresyl violet, and coverslipped using Permount (Fisher Scientific, Pittsburgh, PA).

2.5 Cochlear Nucleus Reconstruction and Analysis Region

Each CN was reconstructed and manipulated in 3D following previously described methods (Muniak et al., 2013). Briefly, serial sections through the entire CN ipsilateral to the AN injection were photographed with a light microscope and manually aligned in *Photoshop* (Adobe Systems, San Jose, CA) using blood vessels and other tissue landmarks to re-establish continuity along the anterior-posterior axis. Once aligned, the area of the entire CN, as well as the dorsal and ventral subdivisions (DCN and VCN, respectively), were each segmented using a graphics tablet (Cintiq 12WX; Wacom, Vancover, WA) following standard criteria (Willard and Ryugo, 1983). These outlines were exported as image-stacks and used to compute 3D surfaces for each case using *Amira* software (Visage Imaging, San Diego, CA). Because the entirety of the CN was not included in all cases (e.g., exclusion of posterior-most sections of the DCN), the 3D reconstruction of each case was left unbounded (i.e., not "closed") at the anterior and posterior ends of the surface. Doing so ensured that *Amira* did not attempt to force artificial edges into alignment with the target surface. Separate reconstructions of the VCN, however, were complete and thus "closed". Each experimental 3D CN surface was then aligned to the 3D template of the CN frequency model (Muniak et al., 2013) using affine transformations in *Amira*. The quality of each fit was quantified using the root mean square (RMS) distance of vertices of the experimental surface to the template surface. Estimated VCN volumes were computed in *Amira* both before and after applying the computed transformation. The transformation matrix was then used to map the coordinates of all labeled pixels in each DCN and VCN image-stack to

the coordinate-space of the frequency model, facilitating the prediction of a best frequency for each labeled pixel (http://3d.ryugolab.com/). Using these predictions, a custom *MATLAB* (Mathworks, Natick, MA) routine was used draw the boundaries of the frequency range of interest upon the original image data, thus demarcating the "analysis region" for further study. This region was restricted to the AVCN by excluding all sections at and posterior to the intersection of the AN root with the ventral surface of the CN.

2.6 Immunohistochemistry and Electron Microscopy

Animals used for EM were perfused with either 4% paraformaldehyde or a 2%/2% paraformaldehyde/glutaraldehyde solution in 0.1M phosphate buffered saline solution (pH 7.4; Table 3). Animals with tissue destined for GlyT2 immunostaining were perfused with 4% paraformaldehyde because the primary antibody binding was desensitized by glutaraldehyde. Coronal sections (50 µm thickness) were prepared as described in section 2.4. Following a 10-min 1% H_2O_2 incubation, sections were rinsed and permeabilized with 0.1% PhotoFlo (Kodak, Rochester, NY) in 0.12M TBS for 1 hr, and then incubated in 5% normal goat serum (005-000-121; Jackson Immuno Research Laboratories, West Grove, PA) in 0.12M TBS for 1 hr. Tissue sections were next incubated in a solution of primary antibody, 1% normal goat serum, and 0.1% PhotoFlo in 0.12M TBS overnight on the shaker at 4 ºC. Primary antibodies used were green fluorescent protein (GFP; 1:1000, polycolonal antibody made in rabbit; ab6556; Abcam, Cambridge, UK) and GlyT2 (1:1000, polycolonal antibody made in rabbit; HPA039476; Sigma-Aldrich). The next day, free-floating sections were rinsed in three changes of 0.12M TBS for 5 min each, then incubated for 1 hr at room temperature in a 1:200 goat anti-mouse (BA-9200;

Vector Laboratories) secondary solution in 0.12M TBS. Lastly, sections were developed in a DAB solution (see section 2.4).

To prepare for EM processing, sections were rinsed in 0.1M maleate buffer (pH 5) before a short incubation (~10 min) in 1% osmium tetroxide in 0.1M s-Collidine buffer (pH 7.4). Sections were then rinsed again in maleate buffer and stained overnight in 1% uranyl acetate. This step was followed by additional tissue rinses, graded dehydration in alcohols and propylene oxide, and embedding in PolyBed 812 (Polysciences Inc., Warrington, PA). Sections were then sandwiched between two sheets of Aclar (Electron Microscopy Sciences, Hatfield, PA), hardened in the oven at 60 ºC, and photographed with the light microscope. Images of the AVCN were matched to similar sections from reconstructed 3D cases (see section 2.5) in order to estimate the relevant "analysis region" in these cases. Next, small sections of the AVCN containing only analysis regions were cut away from the resin embedded tissue, and re-embedded in PolyBed 812 in BEEM capsules for ultramicrotome sectioning. Sections were cut at 75 nm thickness, collected on Formvar-coated copper grids, and stained with uranyl acetate and lead citrate before photographing BCs with a transmission EM (H7650; Hitachi, Tokyo, JPN). BCs were identified using previously established criteria: round-to-oval cell bodies, pale nucleus, and the presence of a perinuclear Nissl cap (Cant and Morest, 1979). All discernable BCs within random sections through AVCN analysis regions were imaged.

2.7 Data Analysis

All tissue was coded prior to analysis so that the observer was blinded to age and strain of subjects. The mean width of each VCN was computed in *MATLAB* through a series of image processing routines. First, a 1-pixel-wide topological skeleton of the binary image of a

segmented VCN section was computed using a “thinning” algorithm. The largest shortest path of this skeleton was then determined, and all branches not belonging to this path were pruned. Lastly, a Euclidean distance transform of the source binary image was computed, and the values for all pixels that intersected with the pruned topological skeleton were multiplied by 2 and saved. The mean VCN width consisted of the calibrated mean of all distance values from all VCN sections of a given case. To estimate the VCN width following alignment to the CN template, the percent change in VCN volume before and after the transformation was determined, and the cube root of this percentage was multiplied by the non-transformed mean VCN width.

Neurolucida software (MBF Bioscience, Williston, VT) was used for online slide analysis of AVCNs ipsilateral to the AN injection. The entire CN was outlined in each section and the previously computed “analysis region” (see section 2.5) was overlaid. BCs and EBs residing within the analysis region were traced using previous descriptions (Lauer et al., 2013; Lorente de Nó, 1981; Ryugo and Fekete, 1982). BCs stained by 1% cresyl violet were identified based on their location in the AVCN and round-to-oval shape with a centrally placed nucleus. EBs were defined as large endings in the AVCN composed of a primary stalk that bifurcates into many smaller stalks and forms *en passant* and bouton endings onto the BC soma. Data are reported as BC area and EB silhouette area. To estimate the geometric complexity of each EB, the shape factor, *s*, of the silhouette was calculated using the formula: $s = p/\sqrt{a}$, where p and a are the perimeter and area of the silhouette, respectively.

EM micrographs of BCs were montaged and analyzed using *TrakEM2* software (Cardona et al., 2012) and *Shape Analysis*, a custom suite of Python and MATLAB routines for geometric analysis of objects in *TrakEM2* (Michael Muniak). Ultrastructural features were segmented

within *TrakEM2* using a graphics tablet (Cintiq 22HD; Wacom). Sections stained for GFP or GlyT2 were used to analyze unstained terminal ultrastructure. These stains allowed us to exclude inhibitory terminals from analysis. Terminal area, terminal apposition, mitochondrial fraction, and synapse length and curvature were quantified. As the exact plane at which BCs were sectioned varied relative to the mid-nuclear point, data values were normalized to the BC sample. Thus, total terminal area was divided by BC area, and total apposition length was divided by BC perimeter. Mitochondrial fraction was calculated by dividing the total area of mitochondria within terminals by total terminal area per cell. Synapse curvature, *c*, was defined as the inverse of the radius of an imaginary arc with width *w* and height *h*, where *w* is the length of the chord connecting the endpoints of the synapse curve and *h* is the maximum orthogonal distance of the synapse curve from the chord, taking the form: $c = (h/2 + w^2/(8h))^{-1}$ (Cooke et al., 1974).

2.8 Statistical Analysis

Statistics were calculated using *Prism* software (GraphPad Software, La Jolla, CA). ABR thresholds at each frequency, as well as CN size and alignment metrics, from each strain and age were compared using a one-way ANOVA and Holm-Sidak's multiple comparisons correction test with a single pooled variance. All other metrics (area, shape factor, etc.) consisted of multiple measurements from 2-4 animals in each cohort. Due to inconsistent numbers of measurements that could be obtained from each animal (a fact not apparent during blinded analyses), we pooled all measurements from all animals within a given cohort when making statistical comparisons to other cohorts. Generally, data values were not normally distributed according to the D'Agostino & Pearson omnibus normality test. Therefore, non-parametric testing was performed on these

datasets using the Kruskal-Wallis one-way ANOVA. Post-hoc pairwise comparisons were performed using Dunn's multiple comparisons test. For all tests, comparisons were made between all possible combinations of strain and age, and significance was determined using multiplicity-adjusted p-values. Significant findings from less meaningful comparisons (e.g., 6-mo. CBA/Ca vs. 1-mo. DBA/2) have been omitted from the results. As variance within a cohort could have an effect on the results, we also tested for significant differences between animals within a cohort using the Mann-Whitney (for cohorts with only 2 subjects) or Kruskal-Wallis/Dunn's tests as above. All error values are reported as mean ± standard deviation (SD) unless otherwise indicated.

3. RESULTS

3.1 Auditory Brainstem Responses

All subjects appeared healthy, with normal tympanic membranes and no evidence of external or middle ear infection. ABR thresholds to clicks and tones for CBA/Ca mice were consistent with previous reports (Willott, 1986; Zheng et al., 1999) and did not significantly differ with age (Fig. 1). Only click responses had been previously reported for hearing *sh2*$^{+/-}$ mice (Lee et al., 2003; Limb and Ryugo, 2000), and these values were matched by present results. While thresholds to clicks did not vary with age for *sh2*$^{+/-}$ mice (Fig. 1), their audiograms did significantly differ from that of CBA/Ca mice, showing elevated thresholds at 24, 32, and 40 kHz, and lower thresholds at 4 kHz, for 3- and 6-month cohorts. Deaf *sh2*$^{-/-}$ mice had no evoked response to sound at any age.

ABR thresholds for DBA/2 mice were also consistent with previous studies (Johnson et al., 2000; McGuire et al., 2015; Wang and Manis, 2006; Willott and Turner, 1999; Zheng et al.,

1999). At 1 month of age, a high frequency hearing loss was evident that was significantly elevated compared to CBA/Ca thresholds at 24, 32, and 40 kHz (Fig. 1). By 3 months, DBA/2 thresholds were significantly elevated from CBA/Ca levels at all frequencies except for 4 kHz, and by 6 months these mice were profoundly deaf at all tested frequencies. When compared to the 1-month DBA/2 cohort, older DBA/2 mice showed elevated thresholds at 8 kHz (3- and 6-mo., $p \leq 0.0001$), 16 kHz (3- and 6-mo., $p \leq 0.0001$), 24 kHz (3-mo., $p \leq 0.05$; 6-mo., $p \leq 0.01$), and 32 kHz (3- and 6-mo., $p \leq 0.01$). Of these frequencies, only 8- and 16-kHz thresholds at 1 month were comparable to CBA/Ca thresholds, suggesting that these frequencies exhibited the greatest variation—from normal hearing to profound loss—for auditory thresholds across age in DBA/2 mice. Therefore, we chose an octave-band centered on 12 kHz as the frequency range used to define the "analysis region" in the AVCN for all subsequent anatomical analyses (see section 2.5).

3.2 Cochlear Nucleus Reconstructions and Analysis Region

Coronal image-stacks of the CN were used to reconstruct each nucleus in 3D (Fig. 2A-B). Each 3D CN surface was qualitatively similar in appearance to the template CN (Fig. 2C), however slight differences in VCN volume were evident across mouse strains (Table 1). Grouped across age, the mean VCN volumes for CBA/Ca (0.315 ± 0.038 mm^3) and *sh2*$^{+/-}$ (0.315 ± 0.025 mm^3) mice were significantly larger than DBA/2 mice (0.244 ± 0.029 mm^3; $p \leq 0.01$), but not *sh2*$^{-/-}$ mice (0.275 ± 0.028 mm^3). Linear regression showed a modest increase in VCN volume with age ($R^2=0.17$, $p \leq 0.05$) and weight ($R^2=0.21$, $p \leq 0.05$), but only when all strains were grouped together. Within each strain, there were no significant trends, suggesting that

differences in VCN size could be due to genotypic differences rather than hearing status, albeit sample numbers were low.

All cases fit relatively well to the template CN. Visual inspection of each alignment was agreeable, and fit quality was quantified with an average RMS distance error of 45.8 ± 7.2 μm (n=26; Table 1). Interestingly, CBA/Ca mice had significantly better fits to the template CN (mean RMS error: 38.6 ± 3.7 μm) compared to DBA/2 (48.8 ± 7.0 μm; $p \leq 0.01$) or *sh2*$^{-/-}$ (50.9 ± 5.9 μm; $p \leq 0.01$) mice; the low sample number of *sh2*$^{+/-}$ mice (45.8 ± 3.1 μm) eluded significance. This result was not particularly unexpected, as the template CN was constructed using CBA mice (Muniak et al., 2013). However, given that the template alignment process was intended to "normalize" CN size—indeed, VCN volumes were no longer significantly different across strains (overall average: 0.290 ± 0.021 mm^3)—some other aspect of CN morphology likely contributed to the poorer fits in other mice. Qualitative observations of aligned CN surfaces suggested that non-CBA/Ca CNs sometimes appeared "thinner" than the template CN along the lateral-medial axis. To quantify this trend, we computed the "width" of the VCN by calculating the thickness of each section orthogonal to its long axis (typically an approximation of the dorsal-ventral axis; see section 2.7). Prior to alignment/normalization, CBA/Ca VCNs were significantly "thicker" (Table 1; mean: 198.3 ± 11.2 μm) than in DBA/2 (168.4 ± 13.3 μm; $p \leq 0.001$) or *sh2*$^{-/-}$ (177.7 ± 10.4 μm; $p \leq 0.01$) mice, mirroring VCN volume results. Additionally, *sh2*$^{+/-}$ VCNs (194.5 ± 0.4 μm) were also significantly wider than in DBA/2 mice ($p \leq 0.01$). After adjusting for alignment/normalization to the template, CBA/Ca VCNs remained significantly thicker (mean: 195.9 ± 9.3 μm) than in DBA/2 (177.4 ± 16.4 μm; $p \leq 0.05$) or *sh2*$^{-/-}$ (178.6 ± 10.9 μm; $p \leq 0.05$) mice, but not in *sh*$^{+/-}$ mice (191.1 ± 7.7 μm). Thus, the narrower VCNs in many

non-CBA/Ca mice may account for less precise fits to the template CN, even though overall morphology was comparable.

Following alignment, each CN surface was compared to the 3D frequency model of the mouse CN (Fig. 2C; Muniak et al., 2013). All interior voxels of the CN surface that intersected with the 12-kHz octave-band frequency analysis region were determined (Fig. 2D), and a reverse transformation (inverse of the affine CN alignment) was applied, enabling us to create an overlay of the analysis region upon each section of the source CN image-stack (Fig. 2E). A laminar isofrequency band of our analysis region was thus estimated for each experimental case, with the general appearance of this laminar band being qualitatively similar across all cases. At the anterior edge of the AN root, the band was located near the ventral surface, oriented along a ventromedial to dorsolateral angle, and spanned approximately 15-25% the total section height. At progressively more anterior sections, this band became more horizontal and gradually shifted upwards relative to the bounds of the CN until it eventually tended to occupy the upper half of the anterior tip of the AVCN. All subsequent analyses were restricted to cells and endings located within this laminar region.

3.3 Bushy Cells

BCs were identified based on published criteria (Lauer et al., 2013; Martin, 1981; Willard and Ryugo, 1983), and were found throughout the AVCN analysis region rostral to the AN root. They had round-to-oval somata with a central or slightly eccentric nucleus (Fig. 3). Only BCs with a visible nucleus were considered for analysis. Moreover, the presence of the nucleus suggested that we were viewing the maximum profile of the cell and thus could reliably draw its equatorial perimeter. BCs in which the cell perimeter could not be reliably outlined (e.g.,

obscured by labeled EBs) were excluded from analysis. Because of the stringent criteria applied during blinded analysis, it was impossible to know how many samples were obtained from each animal until all analyses were completed. This circumstance sometimes led to unbalanced distributions of samples between animals of a given cohort, leading us to pool together all measurements within a cohort when making comparisons to other cohorts (also applies to subsequent measurements; see section 2.8).

At 1 month of age, there was no difference in mean cell size across strains (Fig. 4; Table 2; grand mean: 207.8 ± 27.8 μm^2; n=147), suggesting that the initial developmental growth of BCs was not hindered by peripheral hearing loss at such an early stage. As animals aged, however, clear trends related to hearing loss emerged (Fig. 4; Table 2). CBA/Ca and *sh2*$^{+/-}$ mice, which either maintained normal hearing or exhibited relatively minor losses at high frequencies with age, showed no significant change in BC size within or between strains with age. In contrast, both hearing-impaired DBA/2 and deaf *sh2*$^{-/-}$ mice exhibited significantly reduced BC size at both 3 months ($p \leq 0.01$) and 6 months (DBA/2: $p \leq 0.001$; *sh2*$^{-/-}$: $p \leq 0.0001$) of age when compared to their 1-month-old counterparts. Additionally, when compared to age-matched CBA/Ca mice, BCs from 3-month *sh2*$^{-/-}$ ($p \leq 0.001$) and 6-month DBA/2 and *sh2*$^{-/-}$ ($p \leq 0.0001$) mice were significantly smaller. Furthermore, compared to hearing *sh2*$^{+/-}$ subjects, BCs in deaf *sh2*$^{-/-}$ mice were smaller at both 3 months ($p \leq 0.01$) and 6 months ($p \leq 0.0001$). Significant variation in cell size measurements was observed within CBA/Ca, DBA/2, and *sh2*$^{-/-}$ mouse cohorts at 6 months of age. The range of measurements overlapped between subjects in each of these groups with no clear outliers, making it difficult to determine if one or more anomalous subjects may have biased significant outcomes. Despite this variation, these data suggest that a prolonged absence of sound-evoked activity affects BC morphology, resulting in cell atrophy.

While not statistically significant, the greater reductions observed in *sh2*$^{-/-}$ mice compared to DBA/2 mice (Fig. 4B) further suggest that the duration and degree of sound deprivation (e.g., elevated thresholds vs. deafness) may influence the severity of BC atrophy.

3.4 Endbulbs of Held

EBs were identified based on published criteria (Limb and Ryugo, 2000; Lorente de Nó, 1981; Ryugo and Fekete, 1982). In all animals, EBs were larger than other endings in the AVCN. They were composed of a primary stalk that gave rise to a range of complex arborizations that exhibited multiple *en passant* and terminal swellings (Figs. 5-6). EBs in animals with hearing loss, particularly older DBA/2 and *sh*$^{-/-}$ mice, appeared smaller than those from hearing animals (Figs. 5-6), which we quantified using EB silhouette area (Fig. 6). Results from this analysis were comparable to those of BC size (Fig. 7A-B; Table 2). There was no difference in EB area across cohorts at 1 month of age, and CBA/Ca mice showed no change in EB size over time. EBs from *sh2*$^{+/-}$ mice were slightly reduced at 6 months relative to their 3-month counterparts ($p \leq 0.05$), and 6-month-old CBA/Ca and *sh2*$^{+/-}$ mice both showed increased variability for EB size. At 6 months of age, when DBA/2 mice were profoundly deaf, EB silhouettes were significantly smaller than their 1-month peers ($p \leq 0.0001$). Similarly, EBs from both 3-month and 6-month deaf *sh2*$^{-/-}$ mice were significantly reduced compared to their 1-month counterparts ($p \leq 0.0001$), as well as hearing aged-matched CBA/Ca (3-mo.: $p \leq 0.0001$; 6-mo.: $p \leq 0.01$) and *sh2*$^{+/-}$ ($p \leq 0.001$) EBs. CBA/Ca mice at 1 month as well as CBA/Ca and *sh2*$^{-/-}$ mice at 6 months of age showed significant variation within their cohorts. There were no clear outliers in the 1-month CBA/Ca or 6-month *sh2*$^{-/-}$ groups, but one subject with only 5 samples clearly differed from others within the 6-month CBA/Ca cohort. Exclusion of this subject did not reduce

significance with age-matched *sh2*$^{-/-}$ mice but instead suggested a newfound significant difference with 6-month DBA/2 mice. These results support the idea that both the degree and duration of hearing loss have an effect on EB atrophy, with increased amounts of hearing loss resulting in greater reductions in EB size.

In addition to size, prolonged hearing loss is known to have other effects on EB morphology, with EBs from hearing subjects exhibiting more complex arborizations compared to hard-of-hearing and deaf animals (Limb and Ryugo, 2000; Ryugo et al., 1997, 1998). To explore this idea in our dataset, we calculated the shape factor of each EB silhouette, where larger values indicate more complex contours relative to surface area. In all hearing and partial-hearing strains, there appeared to be no significant difference in EB complexity between the youngest (1-mo.) and oldest (6-mo.) time points (Fig. 7C-D; Table 2). Curiously, both CBA/Ca and DBA/2 mice exhibited a transient increase in EB complexity at 3 months (3-mo. vs. 6-mo. CBA/Ca: $p \leq 0.01$; 3-mo. vs. 1-mo. DBA/2: $p \leq 0.05$), suggesting some sort of developmental or age-related process may be present, although this growth burst was not observed in hearing *sh2*$^{+/-}$ mice. Notably, EBs in deaf *sh2*$^{-/-}$ mice showed a clear progressive reduction in complexity with prolonged deafness, both when compared to earlier strain-matched age points (1-mo. vs. 6-mo.: $p \leq 0.001$; 3-mo. vs. 6-mo.: $p \leq 0.05$) as well as to age-matched CBA/Ca (3-mo.: $p \leq 0.001$; 6-mo.: $p \leq 0.05$) and *sh2*$^{+/-}$ (6-mo.: $p \leq 0.001$) mice. However, significant within-subject variability was observed in a number of cohorts (Fig. 7). In particular, for 1-month *sh2*$^{+/-}$ as well as 6-month CBA/Ca and DBA/2 mice, there was a lack of overlap in the range of values between subjects leading to a wide range of values in their pooled datasets. It was unclear if subjects with higher or lower shape factor values were anomalous, or if these samples reflected normal variety in the population. As such, some of the significant differences regarding shape factor measurements

should be viewed with caution. Importantly, the differences between hearing and deaf 6-month *sh2* mice or 1- and 6-month-old *sh2*$^{-/-}$ mice were not called into question. These findings indicate that both age and neural activity influence EB morphology, with prolonged inactivity in the AN resulting in EB atrophy.

3.5 Bushy Cell Ultrastructure

Ultrastructural studies were conducted on 3- and 6-month-old cohorts from all strains, focusing on BCs and their somatic inputs (Table 3). All identifiable BCs (criteria of Lauer et al., 2013; Lee et al., 2003) within the designated analysis region were photographed and analyzed. Cells were round to oval in shape, with a centrally placed pale nucleus, often with prominent nucleoli visible. The nucleus was usually round with no invaginations other than an occasional small infolding of the nuclear membrane. In many sections through the BC, a cap of Nissl substance could be seen in the cytoplasm tightly bordering the nuclear membrane. Examples of BC drawings from all cohorts are shown in Figure 8 (blue). The cross-sectional area of each BC was measured, however no clear relationship with hearing status or age was evident—these values were more random and always smaller than those measured at the light microscope. For example, the mean cross-sectional BC area of 3-month- and 6-month-old CBA/Ca mice was 147.0 ± 29.7 μm^2 and 164.4 ± 43.8 μm^2, respectively, each ~50 μm^2 smaller than similar light-microscopic measures (compare to Table 2). This result is not surprising, as processing for EM invariably results in tissue shrinkage (Korogod et al., 2015). Additionally, a single EM section is unlikely to capture the equatorial perimeter so that the resulting outline will underestimate the maximum cell profile.

BC somata received numerous axosomatic terminals that covered much of the cell membrane. To help disambiguate between different types of synaptic terminals contacting BCs (i.e., excitatory vs. inhibitory), we employed transgenic GlyT2-EGFP mice, which express EGFP in glycinergic neurons. EGFP expression in the AVCN was evident in cell bodies as well as axonal and dendritic processes, as previously described (Simat et al., 2007; Zeilhofer et al., 2005). Immunohistochemistry for EGFP enabled us to selectively label glycinergic terminals surrounding BCs with medium (Fig. 9A) to dense (Fig. 9B) amounts of reaction product that filled the cytosol, but not the vesicle lumen. As transgenic DBA/2 mice were unavailable for study, we used GlyT2 immunohistochemistry in these animals, resulting in analogous, albeit less dense, terminal labeling (Fig. 9C). Unlabeled terminals in all cases were easily distinguished from darkly stained glycinergic endings (Fig. 9A-C), and most, if not all, were presumed to belong to excitatory EBs: they contained large round vesicles, curved PSDs, and cisternae—all characteristics of AN fibers (Fig. 9D; Baker et al., 2010; Cant and Morest, 1979; Lauer et al., 2013; Lee et al., 2003; O'Neil et al., 2010; Ryugo et al., 1997, 1998).

3.6 Unlabeled Axosomatic Terminals and Synapses

The area constrained within the presynaptic membrane of unlabeled terminals surrounding BCs was outlined and measured (Fig. 8; green). If a part of the axon process was attached, it was excluded based on the presence of neurofilaments. As all BC sections contained a nucleus, we assumed we were analyzing terminals near the midline of the BCs (Fig. 8). However, because the sections were so thin (70-75 nm), measurements from electron micrographs were even more variable than anticipated, with profiles being highly irregular in size. As a result, total terminal profile area and apposition were normalized to the area or

perimeter, respectively, of the associated BC. Following this correction, we found that there was no change over time in unlabeled axosomatic terminal area for hearing and partial-hearing animals (Fig. 10A). In contrast, deaf *sh2*$^{-/-}$ mice showed a significant reduction in this value from 3 to 6 months ($p \leq 0.05$). Furthermore, while only one CBA/Ca sample produced a normalized terminal area greater than 0.2, values from all hard-of-hearing and deaf cohorts were considerably more wide-ranging (Fig. 10A). Variability was noted within 6-month CBA/Ca and 3-month *sh2*$^{+/-}$ groups, but this did not appear to affect outcomes. Note, in particular, the increase both in mean value ($p \leq 0.05$) and variance at 3 months in deaf *sh2*$^{-/-}$ mice relative to hearing *sh2*$^{+/-}$ mice. Similarly, the amount of unlabeled terminal apposition to the BC significantly greater in DBA/2 and *sh2*$^{-/-}$ mice at 3 months of age relative to age-matched CBA/Ca subjects (Fig. 10B; $p \leq 0.0001$), as well as between 3-month hearing and deaf *sh2* subjects ($p \leq 0.05$). However, by 6 months, total apposition in *sh2*$^{-/-}$ mice reduced ($p \leq 0.01$), with a pair of BCs showing less than 15% unlabeled terminal coverage. A single outlier was present in both 3-month *sh2* cohorts, producing significant variability within these groups. Inclusion of these subjects did not appear to bias our results. In combination, these findings suggest that, with reduced sound-evoked activity, some non-glycinergic terminals on BCs may become enlarged, but with prolonged inactivity, these terminals ultimately begin to decrease in size and contact.

Results for mitochondrial fraction in unlabeled terminals were more difficult to interpret (Fig. 10C). At 3 months, the mitochondrial fraction was either greater (*sh2*$^{+/-}$: $p \leq 0.05$) or smaller (*sh2*$^{-/-}$: $p \leq 0.05$) than in CBA/Ca mice. However, relative to 6-month CBA/Ca mice, this value was smaller for all other strains (*sh2*$^{+/-}$ & DBA/2: $p \leq 0.01$; *sh2*$^{-/-}$: $p \leq 0.05$). There was significant variability between 3-month *sh2*$^{-/-}$ subjects that may have contributed to the difference with age-

matched CBA/Ca mice. Only within hearing *sh2*$^{+/-}$ mice did the mitochondrial fraction significantly differ between age points ($p \leq 0.001$), casting doubt on any correlation with hearing status.

Synapses in unlabeled terminals surrounding BCs were identified in all cohorts by the presence of electron dense thickenings on the pre- and postsynaptic membranes, a distinct synaptic cleft between the membranes, and the presynaptic accumulation of synaptic vesicles (Fig. 11). The postsynaptic thickening, or PSD, was routinely markedly thicker than that of the presynaptic membrane, giving the specialization a distinctly asymmetric appearance associated with excitatory EB input (e.g., Cant and Morest, 1979; Lenn and Reese, 1966). There was no apparent difference in the mean number of PSD profiles per cell across or within cohorts (Table 3). After normalizing this value to cell size (dividing by BC perimeter), only 3-month-old *sh2*$^{-/-}$ mice showed a slight increase in PSD density relative to their hearing *sh2*$^{+/-}$ counterparts ($p \leq 0.05$).

As with terminals, the total amount of unlabeled terminal PSD apposition was normalized with respect to BC perimeter. Following this adjustment, the only notable difference was an increase in PSD apposition between 3-month hearing and deaf *sh2* mice (Fig. 12A; $p \leq 0.01$), a change that disappeared in older animals. Absolute PSD length was also relatively similar across all cohorts (Fig. 12B). Only a slight increase between 3-month hearing and deaf *sh2* mice ($p \leq 0.01$) and a slight decrease between CBA/Ca and DBA/2 mice ($p \leq 0.001$) reached significance, but given their opposite trends and the wide range of values observed (Fig. 12A), it is difficult to ascribe these changes to differences in hearing status. Furthermore, despite overlapping value ranges, significant variability was observed in all 3-month-old cohorts, which could have biased comparisons.

An array of PSD profile shapes were observed in all animal cohorts (Fig. 11). Synapses usually had concave presynaptic membranes, protruding into the presynaptic terminal, a common feature of EB terminals (Baker et al., 2010; Cant and Morest, 1979; Lauer et al., 2013; Lee et al., 2003; O'Neil et al., 2010; Ryugo et al., 1997, 1998). Nonetheless, this curvature was quite variable and not always concave into the terminal—some PSDs were flattened, and only rarely appeared convex. Quantification of PSD curvature revealed that PSDs in hearing *sh2*$^{+/-}$ mice were significantly more curved than in age matched deaf *sh2*$^{-/-}$ animals (Fig. 12C; $p \leq 0.0001$). Variability was observed between subjects within both CBA/Ca cohorts, as well as within the 3-month *sh2*$^{+/-}$ and 6-month *sh2*$^{-/-}$ cohorts, and the latter may have contributed to the lone significant comparison. While not significant, PSDs in all hearing cohorts were on average more curved than in hearing-loss groups, and 6-month-old animals with hearing loss had flatter PSDs compared to their strain-matched 3-month-old cohorts (Table 3).

4. DISCUSSION

In this study, we examined the effects of progressive hearing loss on the EB-BC interface in the AVCN. It was hypothesized that a reduction of sound-evoked activity in the AN would result in definable pathological changes in these structures, with the cumulative effect of both magnitude and duration of hearing loss causing more pronounced changes to normal structure. We contrasted two hearing mouse strains (CBA/Ca and heterozygous *sh2*$^{+/-}$) against a congenitally deaf strain (*sh2*$^{-/-}$) and a model of progressive early-onset hearing loss (DBA/2). It is important to note here that the heterozygous *sh2*$^{+/-}$ mice did not have normal hearing. Although previous studies showed normal thresholds with click stimuli (Lee et al., 2003; Limb and Ryugo, 2000), our results indicate that they have a high frequency hearing loss. By 3

609 months of age, they had a 40-dB loss at 24 kHz, 55-dB loss at 32 kHz, and no detectable hearing
610 at 40 kHz. Hearing loss at 6 months of age was 50 dB or greater above 24 kHz.
611 We utilized a model of frequency representation in the mouse CN (Muniak et al., 2013) to
612 concentrate our morphological analyses to a frequency region that exhibited the most graded
613 change in DBA/2 hearing thresholds with age and remained stable for hearing animals. Under
614 the light microscope, there were clear effects on both EB and BC morphology, with prolonged
615 and/or more severe hearing loss resulting in greater atrophic changes. However, hearing loss
616 produced less dramatic consequences to ultrastructure, with minor effects seen in total terminal
617 profile area and apposition but not PSDs. These results support the idea that EBs and BCs are
618 sensitive not only to complete sensory deprivation, but also degraded AN activity as a result of
619 partial hearing loss.
620
621 **4.1 Frequency-Specific Analyses**
622 Frequency-specific damage in the cochlea leads to topographic damage in the CN (Bilak
623 et al., 1997; Morest and Bohne, 1983; Morest et al., 1998; Willott et al., 1982). Peripheral insult
624 to AN fibers and/or their associated hair cell receptors results in the degeneration of their central
625 axonal processes. These changes are not observed in AN fibers connected to undamaged
626 cochlear regions. As such, one cannot treat the CN as a single homogenous structure when
627 studying the effects of a partial hearing loss. Indeed, prior studies of animals with a high-
628 frequency hearing loss have made efforts to restrict their region of analysis in the CN to areas
629 presumed to be most affected by the loss (Helfert et al., 2003; Wang and Manis, 2006; Willott
630 and Bross, 1996). These studies, however, made their estimates visually. While such
631 approximations can certainly reduce variability in the data set, the recent frequency model of the

mouse CN (Muniak et al., 2013) makes it clear that frequency organization throughout the CN is fluid and shifting. In our coronal CN sections, the 12-kHz-centered octave-band shifted from ventral locations in the posterior AVCN to more dorsal locations in the anterior AVCN. A "best guess" estimation of this frequency zone would have been inaccurate had we chosen to study only the ventral portion of the AVCN because regions representing lower but normal frequencies would have been unnecessarily included. By utilizing the 3D model of frequency representation in the CN (Muniak et al., 2013), we were able to confidently restrict our analyses to the desired region of interest.

As the CN model was developed in CBA mice (Muniak et al., 2013), its use in our study does raise an important consideration: how consistent is frequency representation in the CN of mouse strains of different genetic backgrounds, especially those with progressive hearing loss or congenital deafness? Our reconstructions suggest that only minor differences may exist with respect to gross CN shape. The low sample numbers for 3D reconstructions, however, make it difficult to determine whether these differences are due to genotype or hearing status. In normal hearing animals, AN projections into the CN give rise to highly organized frequency lamina throughout the extent of the nucleus (Berglund and Brown, 1994; Fekete et al., 1984; Feng and Vater, 1985; Leake and Snyder, 1989; Muniak et al., 2013). A study of congenitally-deaf *jerker* mice states that the projection of AN fibers into the CN remains narrow and topographic (Cao et al., 2008), although this was only examined in thin slice preparations that would prevent the viewing of any spread that might occur in the nucleus outside the slice. Conversely, quantification of topographic specificity of AN projections into the CN of neonatally-deafened adult cats suggests that, while cochleotopic organization remains grossly preserved, these

projections are broader than in normal-hearing cats after normalizing for CN size (Leake et al., 2006).

Changes to tonotopic organization in the CN of animal models of progressive hearing loss are less well characterized. Physiological recordings along the dorsoventral axis of the VCN in 3-week-old DBA/2 mice revealed a disproportionate representation of units in the mid-frequency range (~12-16 kHz; Willott et al., 1982). It seems unlikely that this expansion is the result of unmasking formerly high-frequency units, as thresholds remained low, and may instead indicate a broadening of AN projections. To unambiguously resolve the question of topographic specificity in animals with hearing loss, careful reconstructions linking the location of AN projections in the CN to their cochlear origin will be required (e.g., Muniak et al., 2013).

If activity-dependent changes to topographic organization do in fact take place in the CN, how might this impact our frequency-specific approach to analysis? Data from CBA/Ca mice should, of course, pose no issue, and barring any evidence to the contrary, it is assumed that tonotopic organization in hearing *sh2*$^{+/-}$ mice is also similar, at least in the range of low- to mid-frequencies. Similarly, any pathologic effects in congenitally deaf *sh2*$^{-/-}$ animals are presumed to occur throughout the CN and should be reflected in whatever region of interest we select. In DBA/2 mice, however, the scenario of topographic reorganization in response to hearing loss could result in the migration of “normal” low-frequency projections into our 12-kHz region of interest that was designed to sample the leading edge of the progressive hearing loss. If anything, such a phenomenon would likely dilute the significance of our findings in DBA/2 mice, as we may have inadvertently included healthy AN processes in our analysis. Nonetheless, we were able to reveal significant atrophic changes to BC and EB morphology in DBA/2 mice following progressive loss.

677

678 **4.2 Bushy Cells**

679 There appears to be a causal relationship between cell size and activity, with increased
680 cell activity leading to an increase in cell size. In male songbirds, cells in the robust nucleus of
681 the arcopallium—a song control nucleus—seasonally increase in spontaneous firing rate and
682 soma size during breeding periods (Meitzen et al., 2007). In the CN, BCs receiving input from
683 high-spontaneous rate AN fibers are larger than those receiving input from low-spontaneous rate
684 fibers (Sento and Ryugo, 1989). Prolonged exposure to a moderate-level tone can also result in
685 somatic enlargements in the auditory cortex and inferior colliculus (Lu et al., 2009, 2014).
686 Conversely, when a system is underactive, cells atrophy. It has been well documented that BCs
687 in the CN shrink when afferent activity is absent in congenitally deaf (Larsen and Kirchhoff,
688 1992; Saada et al., 1996; West and Harrison, 1973) or cochlear-ablated (Born and Rubel, 1985;
689 Hashisaki and Rubel, 1989; Moore, 1990; Pasic and Rubel, 1989; Powell and Erulkar, 1962;
690 Trune, 1982) animals. The same results are also seen in other sensory systems following
691 deprivation of afferent input (Benson et al., 1984; Durham and Woolsey, 1984; Wiesel and
692 Hubel, 1963).

693 Age also plays an important role in determining the magnitude of this effect. Kittens that
694 have been ototoxically deafened as neonates exhibit significantly smaller BCs than those
695 deafened at 1 month of age (Stakhovskaya et al., 2008). A similar phenomenon is evident in our
696 results: BCs from DBA/2 mice become smaller as their hearing deteriorates with age, but greater
697 reductions are observed in congenitally-deaf *sh2*$^{-/-}$ mice. The absence of sensory input prior to
698 maturation clearly has deleterious effects on BC size, but acquired loss also leads to intermediate
699 reductions. The progression of our DBA/2 results matches that of an earlier report from Willott

700 and Bross (1996), where significant reductions in neuron size were not seen until after 1 month
701 of age—when hearing loss accelerates—although specific cell types were not identified. More
702 recent DBA/2 observations noted a non-significant reduction of BCs with age (McGuire et al.,
703 2015), however the younger cohort in this study included 2-month-old mice where BCs may
704 have already begun to atrophy (based on our 1- and 3-month old results). Note also that these
705 earlier studies examined the entire AVCN; our frequency-based analysis was designed to isolate
706 those cells that were most likely to exhibit hearing-dependent changes.
707
708 **4.3 Endbulbs of Held**
709 The large, complex EB is sensitive to changes in AN activity. Classic reports on the
710 congenitally deaf white cat showed that the total absence of sound-evoked activity led to
711 significant EB atrophy relative to normal hearing cats, as well as a marked reduction in axonal
712 branching or complexity (Ryugo et al., 1997, 1998). Similar results have been found in various
713 mouse models of congenital deafness. As in our study, EBs from 2-month-old *sh2*$^{-/-}$ animals
714 appeared smaller and determined to be less complex (via fractal analysis) than those from
715 heterozygous *sh2* littermates or CBA mice (Limb and Ryugo, 2000). Examination of different
716 <1-month-old deaf mutant mice also revealed EB abnormalities: qualitatively smaller EBs in
717 *jerker* mice (Cao et al., 2008), smaller EBs and significantly reduced branching in *otoferlin* mice
718 (Wright et al., 2014), and statistically smaller EB volume in *deafness* mice (Youssoufian et al.,
719 2008). These changes are also not limited to total deafness—quantification of VGlut1-positive
720 puncta surrounding BCs (a proxy for EB terminals) showed reductions in older (9-10 mo.)
721 DBA/2 mice compared to younger (1-2 mo.) subjects (McGuire et al., 2015), a trend that
722 matches our EB silhouette data for DBA/2 animals. It is possible that we may have inadvertently

biased our selection of EBs towards more “normal” looking endings—significantly atrophied EBs may have been dismissed as belonging to passing fibers or different ending type—thus reducing the impact of our results. Significant outcomes were found nonetheless.

The observation of statistically smaller EBs in young *deafness* mice (Youssoufian et al., 2008) raises the question of stunted development vs. atrophy with respect to EB morphology. In all of our normal and hearing-impaired cohorts, EB (and BC) measures were statistically identical at 1 month—atrophic changes were not manifest until later. In the mouse, hearing onset occurs at 2 weeks and ABR thresholds stabilize by 4 weeks (Ehret, 1976) when the EB fully matures (Limb and Ryugo, 2000). One week of true “silence” hardly seems sufficient to explain the small EBs of 3-week-old *deafness* mutants, when in our hands 1-month-old *sh2*$^{-/-}$ animals appear relatively normal. A plausible explanation for this discrepancy may be the presence or absence of spontaneous activity in the AN during development. Prior to hearing onset, ATP-dependent waves of spontaneous activity are generated in cochlear inner hair cells, which in turn cause bursts of firing in AN fibers (Tritsch et al., 2007, 2010). Interestingly, in *deafness* mutants, hair cells appear degenerate from an early age and are likely never functional (Bock and Steel, 1983; Steel and Bock, 1983). In contrast, inner hair cells in *sh2*$^{-/-}$ mice appear relatively normal even at 3 months (Gong et al., 2006). These results support the idea that firing activity in the AN, sound-evoked or otherwise, is necessary for both the normal development *and* maintenance of EB morphology.

4.4 Ultrastructure

Robust changes to ultrastructural features of EBs have been thoroughly documented following congenital deafness (Baker et al., 2010; Gulley et al., 1978; Lee et al., 2003; O'Neil et

al., 2010; Ryugo et al., 1997, 1998). Most prominently, the absence of sound-evoked activity results in the flattening and hypertrophy of normally punctate, dome-shaped PSDs, transformations that are especially prominent in the deaf white cat (Baker et al., 2010; O'Neil et al., 2010; Ryugo et al., 1997, 1998). Such changes may reflect a compensatory response to reduced synaptic transmission and appear to be graded with the amount of activity in the AN: PSDs from low-spontaneous rate fibers are less curved than high-spontaneous rate PSDs (Ryugo et al., 1996), and PSDs from hard-of-hearing cats are intermediate to those of normal and congenitally deaf cats (Ryugo et al., 1998). Accordingly, we expected to find graded changes in our EM measurements that reflected the normal, degraded, and deaf hearing-statuses of our mouse cohorts, reflecting our light microscopic results. Instead, we found a large amount of variability within each cohort that suggests any activity-dependent changes in the mouse EB synapse will be subtle at best. This observation fits with recent qualitative results comparing young and old DBA/2 mice, where no obvious ultrastructural pathologies were observed (McGuire et al., 2015).

Different studies have employed different criteria, methods, and metrics for quantifying EB ultrastructure. In our study, we chose to sample all non-glycinergic endings from numerous BCs throughout the AVCN using single random sections for each cell. The disadvantage to this approach was that we could not reconstruct portions of individual EBs in 3D and measure PSD area, as performed in previous papers (e.g., Lee et al., 2003; Ryugo et al., 1997). However, because the 2D profile length of individual PSDs has also been shown to increase in deaf animals (Baker et al., 2010; Lee et al., 2003; Ryugo et al., 1997), our finding of no obvious change in PSD length was unexpected. Note, however, that the variability in the present and past results was quite large, and each of our measurements was guaranteed to belong to a different synapse

769 rather than being separate cuts through the same ending, which may have diluted our
770 significance. A good part of the variability was that even in long-standing congenitally deaf
771 animals, there were normal-appearing synapses in terms of size, PSD curvature, and synaptic
772 vesicle density. Earlier work on *sh2* mice had also suggested that PSDs flatten in deafness,
773 although this observation was not quantified (Lee et al., 2003). In cat, curvature measures
774 significantly differed between hearing ($3.9 \pm 1.8\ \mu m^{-1}$) and deaf ($1.1 \pm 0.8\ \mu m^{-1}$) cohorts. While
775 small decreases were apparent in our mouse measures with reduced hearing, no statistical
776 significance was observed. In fact, the mean curvature values for each of our cohorts fell in
777 between those reported in cat (range: $1.26 – 2.49\ \mu m^{-1}$; O'Neil et al., 2010), suggesting the
778 "classic" dome-shaped PSD may not be as prominent a feature in mouse EBs, making any
779 potential pathology less obvious. What is clear from our blinded-results is that both PSD length
780 and curvature exhibit broad variations within all cohorts.

781 Another key difference between our study and past approaches is the manner in which we
782 identified EB terminals on BCs using EM. A common approach has been to either directly label
783 EBs with a tracer dye (e.g., Ryugo et al., 1996) or identify unlabeled EBs based on shared
784 characteristics (e.g., Lee et al., 2003; O'Neil et al., 2010). We sought to analyze all terminals
785 surrounding a BC, so injections were not a practical option (complete fills of every EB are
786 unlikely), and we also wanted to reduce subjectivity when classifying endings. Accordingly, our
787 approach of labeling all glycinergic terminals eliminated one of the major sources of somatic
788 inputs to BCs (Altschuler et al., 1986; Wenthold et al., 1988). Because EBs constitute the
789 principal excitatory somatic input to BCs (Cant and Morest, 1979; Ryugo and Sento, 1991), our
790 assumption was that the overwhelming majority of the remaining unlabeled terminals belonged
791 to EBs. A scant number of small GABAergic terminals are reported to contact BC soma (Juiz et

al., 1996; Mahendrasingam et al., 2000, 2004), but they were not selectively identified or excluded for this study because of their infrequent presence and modest modulatory effect on physiological responses (Lim et al., 2000; Nerlich et al., 2014). Other possible sources of non-glycinergic input to BCs have been proposed—local excitatory T-stellate projections (Campagnola and Manis, 2014) and extrinsic cholinergic inputs (Caspary et al., 1983; Oertel and Fujino, 2001)—however it is unclear if these inputs are somatic, and if so, how significant they may be. Because random inspections of our unlabeled terminals consistently fulfill EB criteria such as vesicle size/shape and cisternae, we are comfortable that our measurements are reasonable representations of EB ultrastructure.

4.5 Variability Within Cohorts

When analyzing our data for differences between cohorts, we pooled together measurements from all animals within each cohort prior to making comparisons. This strategy was motivated by the fact that the distribution of measurements was often unbalanced across animals, a fact that was not revealed until all blinded analyses were completed and decoded. We attribute this outcome largely to randomness in the uptake of Neurobiotin by the AN and/or subsequent immunoprocessing, which meant that different cases yielded different numbers of samples that satisfied our criteria for analysis. As a whole, our measurements were largely consistent between animals of a given cohort, supporting our decision to pool data values. When present, significant within-cohort variability did not favor one particular strain or age. Due to the unbalanced distribution of our data, it was not possible to determine if this variation reflected real differences between individual subjects, or instead reflected skewed sampling. As such, we noted when this variability might have impacted our results.

4.6 Functional Implications

The EB and BC provide an important synaptic junction for coding spectral and temporal features of sound, and are considered to be essential for processing timing cues used for sound localization and time-varying cues in speech. Thus, minor perturbations in EB transmission—jitter, delay, or failure—are predicted to disrupt auditory processing. Indeed, transmission irregularities at this interface have been observed both in *deafness* (Oleskevich and Walmsley, 2002) and hard-of-hearing DBA/2 mice (Wang and Manis, 2005, 2006). Impaired temporal processing has also been observed at higher auditory centers in deafened animals (Hancock et al., 2010; Kral et al., 2000), suggesting the effects of reduced AN activity may cascade along the ascending auditory pathway. The reintroduction of AN activity by electrical stimulation from a cochlear implant, however, restores some of these morphological and physiological impairments, although the full benefits of such an intervention are subject to developmental critical periods (Fryauf-Bertschy et al., 1997; Kral and Sharma, 2012; Kral et al., 2001; Niparko et al., 2010; O'Neil et al., 2010; Tirko and Ryugo, 2012).

The observation of progressive morphological changes to EB and BCs in DBA/2 mice highlights a crucial concept that cannot be overstated: acquired hearing loss is not solely a problem of the periphery. The auditory brain is highly sensitive to changes in sensory input, and a failure to intervene results in a degradation of complex auditory functions such as speech recognition in noise. This situation is all the more concerning in the context of acquired hearing loss; if the auditory system is not as reactive to intervention at later stages of life (Kral et al., 2001; O'Neil et al., 2010) effective restoration of function may be greatly hindered. Ultimately, these findings emphasize the importance of protecting one’s hearing throughout their lifetime.

Acknowledgements

We would like to thank Tan Pongstaporn for technical assistance in preparing tissue for electron microscopy, Dr. Amanda Lauer for continued advice throughout the project, and the reviewers for their construct comments on the manuscript. This work was supported by grants from the National Health and Medical Research Council (NHMRC; Grant nos.1080652 and 1081478), the Oticon Foundation (Grant no. 12-1540), the Walker Family Foundation, and gifts from Alan and Lynne Rydge and Haydn and Sue Daw. CJC was a recipient of a University International Postgraduate Award from UNSW Australia.

References

Altschuler, R.A., Betz, H., Parakkal, M.H., Reeks, K.A., Wenthold, R.J. 1986. Identification of glycinergic synapses in the cochlear nucleus through immunocytochemical localization of the postsynaptic receptor. Brain Res 369, 316-20.

Babalian, A.L., Ryugo, D.K., Rouiller, E.M. 2003. Discharge properties of identified cochlear nucleus neurons and auditory nerve fibers in response to repetitive electrical stimulation of the auditory nerve. Exp Brain Res 153, 452-60.

Baker, C.A., Montey, K.L., Pongstaporn, T., Ryugo, D.K. 2010. Postnatal development of the endbulb of held in congenitally deaf cats. Front Neuroanat 4, 19.

Benson, T.E., Ryugo, D.K., Hinds, J.W. 1984. Effects of sensory deprivation on the developing mouse olfactory system: a light and electron microscopic, morphometric analysis. J Neurosci 4, 638-53.

Berglund, A.M., Brown, M.C. 1994. Central trajectories of type II spiral ganglion cells from various cochlear regions in mice. Hear Res 75, 121-30.

Bilak, M., Kim, J., Potashner, S.J., Bohne, B.A., Morest, D.K. 1997. New growth of axons in the cochlear nucleus of adult chinchillas after acoustic trauma. Exp Neurol 147, 256-68.

Bock, G.R., Steel, K.P. 1983. Inner ear pathology in the deafness mutant mouse. Acta Otolaryngol 96, 39-47.

Bogaerts, S., Clements, J.D., Sullivan, J.M., Oleskevich, S. 2009. Automated threshold detection for auditory brainstem responses: comparison with visual estimation in a stem cell transplantation study. BMC Neuroscience 10, 104.

Born, D.E., Rubel, E.W. 1985. Afferent influences on brain stem auditory nuclei of the chicken: neuron number and size following cochlea removal. J Comp Neurol 231, 435-45.

Campagnola, L., Manis, P.B. 2014. A map of functional synaptic connectivity in the mouse anteroventral cochlear nucleus. J Neurosci 34, 2214-30.

Cant, N.B., Morest, D.K. 1979. The bushy cells in the anteroventral cochlear nucleus of the cat. A study with the electron microscope. Neuroscience 4, 1925-45.

Cao, X.J., McGinley, M.J., Oertel, D. 2008. Connections and synaptic function in the posteroventral cochlear nucleus of deaf jerker mice. J Comp Neurol 510, 297-308.

Cardona, A., Saalfeld, S., Schindelin, J., Arganda-Carreras, I., Preibisch, S., Longair, M., Tomancak, P., Hartenstein, V., Douglas, R.J. 2012. TrakEM2 software for neural circuit reconstruction. PloS ONE 7, e38011.

Caspary, D.M., Havey, D.C., Faingold, C.L. 1983. Effects of acetylcholine on cochlear nucleus neurons. Exp Neurol 82, 491-8.

Cooke, C.T., Nolan, T.M., Dyson, S.E., Jones, D.G. 1974. Pentobarbital-induced configurational changes at the synapse. Brain Res 76, 330-5.

Durham, D., Woolsey, T.A. 1984. Effects of neonatal whisker lesions on mouse central trigeminal pathways. J Comp Neurol 223, 424-47.

Ehret, G. 1976. Development of absolute auditory thresholds in the house mouse (*Mus musculus*). J Am Audiol Soc 1, 179-84.

Fekete, D.M., Rouiller, E.M., Liberman, M.C., Ryugo, D.K. 1984. The central projections of intracellularly labeled auditory nerve fibers in cats. J Comp Neurol 229, 432-50.

Feng, A.S., Vater, M. 1985. Functional organization of the cochlear nucleus of rufous horseshoe bats (Rhinolophus rouxi): frequencies and internal connections are arranged in slabs. J Comp Neurol 235, 529-53.

Frisina, R.D., Walton, J.P. 2006. Age-related structural and functional changes in the cochlear nucleus. Hear Res 216-217, 216-23.

Fryauf-Bertschy, H., Tyler, R.S., Kelsay, D.M., Gantz, B.J., Woodworth, G.G. 1997. Cochlear implant use by prelingually deafened children: the influences of age at implant and length of device use. J Speech Lang Hear Res 40, 183-99.

Gong, T.W., Karolyi, I.J., Macdonald, J., Beyer, L., Raphael, Y., Kohrman, D.C., Camper, S.A., Lomax, M.I. 2006. Age-related changes in cochlear gene expression in normal and shaker 2 mice. J Assoc Res Otolaryngol 7, 317-28.

Green, M.C., Witham, B.A. 1991. Handbook on Genetically Standardized JAX Mice. 4th ed. The Jackson Laboratory, Bar Harbor, Maine.

903 Gulley, R.L., Wenthold, R.J., Neises, G.R. 1978. Changes in the synapses of spiral ganglion cells
904 in the rostral anteroventral cochlear nucleus of the waltzing guinea pig following hair cell
905 loss. Brain Res 158, 279-94.
906 Hancock, K.E., Noel, V., Ryugo, D.K., Delgutte, B. 2010. Neural coding of interaural time
907 differences with bilateral cochlear implants: effects of congenital deafness. J Neurosci 30,
908 14068-79.
909 Hashisaki, G.T., Rubel, E.W. 1989. Effects of unilateral cochlea removal on anteroventral
910 cochlear nucleus neurons in developing gerbils. J Comp Neurol 283, 5-73.
911 Helfert, R.H., Krenning, J., Wilson, T.S., Hughes, L.F. 2003. Age-related synaptic changes in the
912 anteroventral cochlear nucleus of Fischer-344 rats. Hear Res 183, 18-28.
913 Henry, K.R., Haythorn, M.M. 1975. Auditory similarities associated with genetic and
914 experimental acoustic deprivation. J Comp Physiol Psychol 89, 213-8.
915 Hultcrantz, M., Spangberg, M.L. 1997. Pathology of the cochlea following a spontaneous
916 mutation in DBA/2 mice. Acta Otolaryngol 117, 689-95.
917 Johnson, K.R., Zheng, Q.Y., Erway, L.C. 2000. A major gene affecting age-related hearing loss is
918 common to at least ten inbred strains of mice. Genomics 70, 171-80.
919 Juiz, J.M., Helfert, R.H., Bonneau, J.M., Wenthold, R.J., Altschuler, R.A. 1996. Three classes of
920 inhibitory amino acid terminals in the cochlear nucleus of the guinea pig. J Comp Neurol
921 373, 11-26.
922 Korogod, N., Petersen, C., Knott, G.W. 2015. Ultrastructural analysis of adult mouse neocortex
923 comparing aldehyde perfusion with cryo fixation. Elife 4:e05793.
924 Kral, A., Sharma, A. 2012. Developmental neuroplasticity after cochlear implantation. Trends
925 Neurosci 35, 111-22.

926 Kral, A., Hartmann, R., Tillein, J., Heid, S., Klinke, R. 2000. Congenital auditory deprivation
927 reduces synaptic activity within the auditory cortex in a layer-specific manner. Cereb
928 Cortex 10, 714-26.
929 Kral, A., Hartmann, R., Tillein, J., Heid, S., Klinke, R. 2001. Delayed maturation and sensitive
930 periods in the auditory cortex. Audiol Neurotol 6, 346-62.
931 Larsen, S.A., Kirchhoff, T.M. 1992. Anatomical evidence of synaptic plasticity in the cochlear
932 nuclei of white-deaf cats. Exp Neurol 115, 151-7.
933 Lauer, A.M., Connelly, C.J., Graham, H., Ryugo, D.K. 2013. Morphological characterization of
934 bushy cells and their inputs in the laboratory mouse (Mus musculus) anteroventral
935 cochlear nucleus. PloS ONE 8, e73308.
936 Leake, P.A., Snyder, R.L. 1989. Topographic organization of the central projections of the spiral
937 ganglion in cats. J Comp Neurol 281, 612-29.
938 Leake, P.A., Hradek, G.T., Chair, L., Snyder, R.L. 2006. Neonatal deafness results in degraded
939 topographic specificity of auditory nerve projections to the cochlear nucleus in cats. J
940 Comp Neurol 497, 13-31.
941 Lee, D.J., Cahill, H.B., Ryugo, D.K. 2003. Effects of congenital deafness in the cochlear nuclei
942 of Shaker-2 mice: an ultrastructural analysis of synapse morphology in the endbulbs of
943 Held. J Neurocytol 32, 229-43.
944 Lenn, N.J., Reese, T.S. 1966. The fine structure of nerve endings in the nucleus of the trapezoid
945 body and the ventral cochlear nucleus. Am J Anat 118, 375-89.
946 Lesperance, M.M., Helfert, R.H., Altschuler, R.A. 1995. Deafness induced cell size changes in
947 rostral AVCN of the guinea pig. Hear Res 86, 77-81.

948 Liang, Y., Wang, A., Belyantseva, I.A., Anderson, D.W., Probst, F.J., Barber, T.D., Miller, W.,
949 Touchman, J.W., Jin, L., Sullivan, S.L., Sellers, J.R., Camper, S.A., Lloyd, R.V., Kachar,
950 B., Friedman, T.B., Fridell, R.A. 1999. Characterization of the human and mouse
951 unconventional myosin XV genes responsible for hereditary deafness DFNB3 and shaker
952 2. Genomics 61, 243-58.
953 Lim, R., Alvarez, F.J., Walmsley, B. 2000. GABA mediates presynaptic inhibition at glycinergic
954 synapses in a rat auditory brainstem nucleus. J Physiol 525 Pt 2, 447-59.
955 Limb, C.J., Ryugo, D.K. 2000. Development of primary axosomatic endings in the anteroventral
956 cochlear nucleus of mice. J Assoc Res Otolaryngol 1, 103-19.
957 Lorente de Nó, R. 1981. The Primary Acoustic Nuclei Raven Press, New York.
958 Lu, H.P., Chen, S.T., Poon, P.W. 2009. Enlargement of neuronal size in rat auditory cortex after
959 prolonged sound exposure. Neurosci Lett 463, 145-9.
960 Lu, H.P., Syka, J., Chiu, T.W., Poon, P.W. 2014. Prolonged sound exposure has different effects
961 on increasing neuronal size in the auditory cortex and brainstem. Hear Res 314, 42-50.
962 Mahendrasingam, S., Wallam, C.A., Hackney, C.M. 2000. An immunogold investigation of the
963 relationship between the amino acids GABA and glycine and their transporters in
964 terminals in the guinea-pig anteroventral cochlear nucleus. Brain Res 887, 477-481.
965 Mahendrasingam, S., Wallam, C.A., Polwart, A., Hackney, C.M. 2004. An immunogold
966 investigation of the distribution of GABA and glycine in nerve terminals on the somata of
967 spherical bushy cells in the anteroventral cochlear nucleus of guinea pig. Eur J Neurosci
968 19, 993-1004.
969 Manis, P.B., Marx, S.O. 1991. Outward currents in isolated ventral cochlear nucleus neurons. J
970 Neurosci 11, 2865-80.

971 Martin, M.R. 1981. Morphology of the cochlear nucleus of the normal and reeler mutant mouse.
972 J Comp Neurol 197, 141-52.
973 McGuire, B., Fiorillo, B., Ryugo, D.K., Lauer, A.M. 2015. Auditory nerve synapses persist in
974 ventral cochlear nucleus long after loss of acoustic input in mice with early-onset
975 progressive hearing loss. Brain Res 1605, 22-30.
976 Meitzen, J., Perkel, D.J., Brenowitz, E.A. 2007. Seasonal changes in intrinsic
977 electrophysiological activity of song control neurons in wild song sparrows. J Comp
978 Physiol A Neuroethol Sens Neural Behav Physiol 193, 677-83.
979 Moore, D.R. 1990. Auditory brainstem of the ferret: early cessation of developmental sensitivity
980 of neurons in the cochlear nucleus to removal of the cochlea. J Comp Neurol 302, 810-
981 23.
982 Morest, D.K., Bohne, B.A. 1983. Noise-induced degeneration in the brain and representation of
983 inner and outer hair cells. Hear Res 9, 145-51.
984 Morest, D.K., Kim, J., Potashner, S.J., Bohne, B.A. 1998. Long-term degeneration in the
985 cochlear nerve and cochlear nucleus of the adult chinchilla following acoustic
986 overstimulation. Microsc Res Tech 41, 205-16.
987 Muniak, M.A., Rivas, A., Montey, K.L., May, B.J., Francis, H.W., Ryugo, D.K. 2013. 3D model
988 of frequency representation in the cochlear nucleus of the CBA/J mouse. J Comp Neurol
989 521, 1510-32.
990 Muniak, M.A., Connelly, C.J., Suthakar, K., Milinkeviciute, G., Ayeni, F.E., Ryugo, D.K. 2016.
991 Central Projections of Spiral Ganglion Neurons. In: Dabdoub, A., Fritzsch, B., Popper,
992 A.N., Fay, R.R., (Eds.), The Primary Auditory Neurons of the Mammalian Cochlea.
993 Springer, New York. pp. 157-190.

994 Nerlich, J., Kuenzel, T., Keine, C., Korenic, A., Rubsamen, R., Milenkovic, I. 2014. Dynamic
995 fidelity control to the central auditory system: synergistic glycine/GABAergic inhibition
996 in the cochlear nucleus. J Neurosci 34, 11604-20.
997 Nicol, M.J., Walmsley, B. 2002. Ultrastructural basis of synaptic transmission between endbulbs
998 of Held and bushy cells in the rat cochlear nucleus. J Physiol 539, 713-723.
999 Niparko, J.K., Tobey, E.A., Thal, D.J., Eisenberg, L.S., Wang, N.Y., Quittner, A.L., Fink, N.E.
1000 2010. Spoken language development in children following cochlear implantation. JAMA
1001 303, 1498-506.
1002 Noben-Trauth, K., Zheng, Q.Y., Johnson, K.R. 2003. Association of cadherin 23 with polygenic
1003 inheritance and genetic modification of sensorineural hearing loss. Nat Genet 35, 21-3.
1004 O'Neil, J.N., Limb, C.J., Baker, C.A., Ryugo, D.K. 2010. Bilateral effects of unilateral cochlear
1005 implantation in congenitally deaf cats. J Comp Neurol 518, 2382-404.
1006 Oertel, D., Fujino, K. 2001. Role of biophysical specialization in cholinergic modulation in
1007 neurons of the ventral cochlear nuclei. Audiol Neurotol 6, 161-6.
1008 Oleskevich, S., Walmsley, B. 2002. Synaptic transmission in the auditory brainstem of normal
1009 and congenitally deaf mice. J Physiol 540, 447-55.
1010 Pasic, T.R., Rubel, E.W. 1989. Rapid changes in cochlear nucleus cell size following blockade of
1011 auditory nerve electrical activity in gerbils. J Comp Neurol 283, 474-80.
1012 Pfeiffer, R.R. 1966. Anteroventral cochlear nucleus: wave forms of extracellularly recorded spike
1013 potentials. Science 154, 667-8.
1014 Powell, T.P., Erulkar, S.D. 1962. Transneuronal cell degeneration in the auditory relay nuclei of
1015 the cat. J Anat 96, 249-68.

Probst, F.J., Fridell, R.A., Raphael, Y., Saunders, T.L., Wang, A., Liang, Y., Morell, R.J., Touchman, J.W., Lyons, R.H., Noben-Trauth, K., Friedman, T.B., Camper, S.A. 1998. Correction of deafness in shaker-2 mice by an unconventional myosin in a BAC transgene. Science 280, 1444-7.

Ryugo, D.K., Fekete, D.M. 1982. Morphology of primary axosomatic endings in the anteroventral cochlear nucleus of the cat: a study of the endbulbs of Held. J Comp Neurol 210, 239-57.

Ryugo, D.K., Sento, S. 1991. Synaptic connections of the auditory nerve in cats: relationship between endbulbs of Held and spherical bushy cells. J Comp Neurol 305, 35-48.

Ryugo, D.K., Spirou, G.A. 2009. Auditory System: Giant Synaptic Terminals, Endbulbs, and Calyces. In: Squire, L.R., (Ed.), Encyclopedia of Neuroscience, Vol. 1. Academic Press, Oxford. pp. 759-770.

Ryugo, D.K., Wu, M.M., Pongstaporn, T. 1996. Activity-related features of synapse morphology: a study of endbulbs of held. J Comp Neurol 365, 141-58.

Ryugo, D.K., Pongstaporn, T., Huchton, D.M., Niparko, J.K. 1997. Ultrastructural analysis of primary endings in deaf white cats: morphologic alterations in endbulbs of Held. J Comp Neurol 385, 230-44.

Ryugo, D.K., Rosenbaum, B.T., Kim, P.J., Niparko, J.K., Saada, A.A. 1998. Single unit recordings in the auditory nerve of congenitally deaf white cats: morphological correlates in the cochlea and cochlear nucleus. J Comp Neurol 397, 532-48.

Saada, A.A., Niparko, J.K., Ryugo, D.K. 1996. Morphological changes in the cochlear nucleus of congenitally deaf white cats. Brain Res 736, 315-28.

1038 Sento, S., Ryugo, D.K. 1989. Endbulbs of held and spherical bushy cells in cats: morphological
1039 correlates with physiological properties. J Comp Neurol 280, 553-62.
1040 Shepherd, R.K., Hardie, N.A. 2001. Deafness-induced changes in the auditory pathway:
1041 implications for cochlear implants. Audiol Neurotol 6, 305-18.
1042 Shin, J.B., Longo-Guess, C.M., Gagnon, L.H., Saylor, K.W., Dumont, R.A., Spinelli, K.J.,
1043 Pagana, J.M., Wilmarth, P.A., David, L.L., Gillespie, P.G., Johnson, K.R. 2010. The
1044 R109H variant of fascin-2, a developmentally regulated actin crosslinker in hair-cell
1045 stereocilia, underlies early-onset hearing loss of DBA/2J mice. J Neurosci 30, 9683-94.
1046 Simat, M., Parpan, F., Fritschy, J.M. 2007. Heterogeneity of glycinergic and gabaergic
1047 interneurons in the granule cell layer of mouse cerebellum. J Comp Neurol 500, 71-83.
1048 Snyder, R.L., Sinex, D.G., McGee, J.D., Walsh, E.W. 2000. Acute spiral ganglion lesions change
1049 the tuning and tonotopic organization of cat inferior colliculus neurons. Hear Res 147,
1050 200-20.
1051 Stakhovskaya, O., Hradek, G.T., Snyder, R.L., Leake, P.A. 2008. Effects of age at onset of
1052 deafness and electrical stimulation on the developing cochlear nucleus in cats. Hear Res
1053 243, 69-77.
1054 Steel, K.P., Bock, G.R. 1983. Hereditary inner-ear abnormalities in animals. Relationships with
1055 human abnormalities. Arch Otolaryngol 109, 22-9.
1056 Tirko, N.N., Ryugo, D.K. 2012. Synaptic plasticity in the medial superior olive of hearing, deaf,
1057 and cochlear-implanted cats. J Comp Neurol 520, 2202-17.
1058 Tritsch, N.X., Yi, E., Gale, J.E., Glowatzki, E., Bergles, D.E. 2007. The origin of spontaneous
1059 activity in the developing auditory system. Nature 450, 50-5.

Tritsch, N.X., Rodriguez-Contreras, A., Crins, T.T., Wang, H.C., Borst, J.G., Bergles, D.E. 2010. Calcium action potentials in hair cells pattern auditory neuron activity before hearing onset. Nat Neurosci 13, 1050-2.

Trune, D.R. 1982. Influence of neonatal cochlear removal on the development of mouse cochlear nucleus: I. Number, size, and density of its neurons. J Comp Neurol 209, 409-24.

Wang, Y., Manis, P.B. 2005. Synaptic transmission at the cochlear nucleus endbulb synapse during age-related hearing loss in mice. J Neurophysiol 94, 1814-24.

Wang, Y., Manis, P.B. 2006. Temporal coding by cochlear nucleus bushy cells in DBA/2J mice with early onset hearing loss. J Assoc Res Otolaryngol 7, 412-24.

Wenthold, R.J., Parakkal, M.H., Oberdorfer, M.D., Altschuler, R.A. 1988. Glycine receptor immunoreactivity in the ventral cochlear nucleus of the guinea pig. J Comp Neurol 276, 423-35.

West, C.D., Harrison, J.M. 1973. Transneuronal cell atrophy in the congenitally deaf white cat. J Comp Neurol 151, 377-98.

Wiesel, T.N., Hubel, D.H. 1963. Effects of Visual Deprivation on Morphology and Physiology of Cells in the Cats Lateral Geniculate Body. J Neurophysiol 26, 978-93.

Willard, F.H., Ryugo, D.K. 1983. Anatomy of the central auditory system. In: Willott, J.F., (Ed.), The Auditory Psychobiology of the Mouse. Charles C Thomas, Springfield, IL. pp. 201-304.

Willott, J.F. 1986. Effects of aging, hearing loss, and anatomical location on thresholds of inferior colliculus neurons in C57BL/6 and CBA mice. J Neurophysiol 56, 391-408.

Willott, J.F., Bross, L.S. 1996. Morphological changes in the anteroventral cochlear nucleus that accompany sensorineural hearing loss in DBA/2J and C57BL/6J mice. Brain Res Dev Brain Res 91, 218-26.

Willott, J.F., Erway, L.C. 1998. Genetics of age-related hearing loss in mice. IV. Cochlear pathology and hearing loss in 25 BXD recombinant inbred mouse strains. Hear Res 119, 27-36.

Willott, J.F., Turner, J.G. 1999. Prolonged exposure to an augmented acoustic environment ameliorates age-related auditory changes in C57BL/6J and DBA/2J mice. Hear Res 135, 78-88.

Willott, J.F., Kulig, J., Satterfield, T. 1984. The acoustic startle response in DBA/2 and C57BL/6 mice: relationship to auditory neuronal response properties and hearing impairment. Hear Res 16, 161-7.

Willott, J.F., Demuth, R.M., Lu, S.M., Van Bergem, P. 1982. Abnormal tonotopic organization in the ventral cochlear nucleus of the hearing-impaired DBA/2 mouse. Neurosci Lett 34, 13-7.

Wright, S., Hwang, Y., Oertel, D. 2014. Synaptic transmission between end bulbs of Held and bushy cells in the cochlear nucleus of mice with a mutation in Otoferlin. J Neurophysiol 112, 3173-88.

Youssoufian, M., Couchman, K., Shivdasani, M.N., Paolini, A.G., Walmsley, B. 2008. Maturation of auditory brainstem projections and calyces in the congenitally deaf (dn/dn) mouse. J Comp Neurol 506, 442-51.

Zeilhofer, H.U., Studler, B., Arabadzisz, D., Schweizer, C., Ahmadi, S., Layh, B., Bosl, M.R., Fritschy, J.M. 2005. Glycinergic neurons expressing enhanced green fluorescent protein in bacterial artificial chromosome transgenic mice. J Comp Neurol 482, 123-41.

Zheng, Q.Y., Johnson, K.R., Erway, L.C. 1999. Assessment of hearing in 80 inbred strains of mice by ABR threshold analyses. Hear Res 130, 94-107.

Figure Legends

Figure 1. Mean ABR thresholds for all animal cohorts. Thresholds for CBA/Ca mice at the frequencies tested are not significantly different across age. Reported significances for all other mice at each frequency are re: age-matched CBA/Ca mice. The shaded vertical bar denotes an octave band centered at 12 kHz. Within this frequency range, DBA/2 mice exhibit the greatest change in hearing threshold over time and 1-month DBA/2 and all $sh2^{+/-}$ mice do not have significantly elevated thresholds re: CBA/Ca values. NR, no response; N, number of animals tested. Bars indicate mean ± SD.

Figure 2. Estimation of 12-kHz-centered octave-band analysis region. (A) Coronal section from a 3-month-old CBA mouse stained for Neurobiotin (brown) and Nissl (blue) with AVCN outlined (red). **(B)** 3D reconstruction of CN from (A), shown from a medial viewpoint. **(C)** 3D frequency model and template of mouse CN (Muniak et al., 2013), shown from a medial viewpoint. **(D)** Estimation of 12-kHz-centered analysis region within experimental CN (B) after alignment to model (C). Location of section from (A) shown with black box. **(E)** Overlay of 12-kHz-centered analysis region (shaded red) on experimental section from (A). All analysis were constrained to this zone. A, anterior; D, dorsal; M, medial.

Figure 3. Examples of bushy cells from all mouse cohorts. Cells are stained for Nissl substance. All analyzed cells in the analysis region expressed characteristics of BCs regardless of the hearing status, including a round-to-oval soma and a round, centrally located nucleus. Somata that were not densely covered by labeled AN fibers were traced.

Figure 4. Bushy cell soma area. **(A)** Individual BC area measurements for each cohort. Bars indicate mean ± SD. Different symbols indicate samples from different subjects. † denotes significant within-cohort variability. **(B)** Mean BC area ± SEM for each cohort compared over time. Asterisks indicate significance re: age-matched CBA/Ca mice. BCs are not significantly different in size across all 1-month-old animals. However, BCs from DBA/2 and sh2$^{-/-}$ mice atrophy over time with hearing loss. **p ≤ 0.01; ***p ≤ 0.001; ****p ≤ 0.0001.

Figure 5. Examples of labeled endbulbs of Held from all mouse cohorts. EBs were labeled with Neurobiotin (brown) and BCs were stained for Nissl substance (blue). EBs from animals with hearing loss are smaller.

Figure 6. Examples of endbulb of Held silhouette tracings from all mouse cohorts. Silhouette tracings of EBs were used to quantify size and complexity. All drawings correspond to EBs shown in Fig. 5. EBs from older animals with hearing loss appear smaller (3- and 6-mo. DBA/2 and *sh2*$^{-/-}$), but maintain their reticulated structure.

Figure 7. Endbulb of Held silhouette measurements. **(A)** Individual EB silhouette area measurements for each cohort. Bars indicate mean ± SD. Different symbols indicate samples from different subjects. † denotes significant within-cohort variability. **(B)** Mean EB silhouette area ± SEM for each cohort compared over time. Asterisks indicate significance re: age-matched CBA/Ca mice. EBs are not significantly different in size across all 1-month-old animals. However, EBs from DBA/2 and *sh2*$^{-/-}$ mice atrophy with over time hearing loss. Atrophic changes are most severe in the 6-month-old *sh2*$^{-/-}$ that experienced the greatest degree and

duration of hearing loss. **(C)** Individual EB silhouette shape factor values for each cohort. Congenitally deaf *sh2*$^{-/-}$ showed a reduction in EB complexity over time. **(D)** Mean EB silhouette shape factor ± SEM for each cohort compared over time. *$p \leq 0.05$; **$p \leq 0.01$; ***$p \leq 0.001$; ****$p \leq 0.0001$.

Figure 8. Examples of bushy cell drawings and their respective unlabeled axosomatic terminals. BCs (cytosol, light blue; nucleus, dark blue) and their respective unlabeled axosomatic terminals (green) were traced from EM micrographs from all cohorts. Qualitatively, no obvious trend in the distribution of terminals was apparent between cohorts.

Figure 9. Ultrastructure of glycinergic and non-glycinergic axosomatic terminals surrounding bushy cells. (A-B) Asterisks denote labeled terminals stained for GFP (A, 6-month-old CBGlyT2; B, 3-month-old *sh2*$^{-/-}$GlyT2). Reaction product was dark and granular within the terminal cytosol, distinguishing glycinergic terminals from unlabeled terminals (green shaded). The density of GFP reaction product within labeled terminals varied case-to-case, independent of fixative solution used for perfusion (A and B, 2%/2% paraformaldehyde/glutaraldehyde fixation). Arrowheads point to the limits of PSDs of unlabeled terminals, which are evidenced by dark postsynaptic membrane thickenings that apposed presynaptic clusterings of synaptic vesicles. It was more difficult to consistently identify PSDs of labeled terminals due to the density of reaction product obscuring membranes and presynaptic vesicle clustering. **(C)** Asterisk denotes labeled terminal stained for GlyT2 (3-month-old DBA/2). The dark granular reaction product tended to appear lighter than GFP label (A-B), but was still visible within the terminal cytosol. **(D)** Unlabeled terminals had characteristics

consistent with AN terminals: they expressed large round vesicles and asymmetric PSDs (between arrowheads) that tended to protrude away from the BC (blue) and curve into the terminal. Unlabeled terminals were also often associated with cisternae (yellow) that arose adjacent to PSDs and are defined as gaps between the pre- and postsynaptic membranes.

Figure 10. Area, apposition, and mitochondrial fraction from unlabeled terminals. (A) Total unlabeled cross-sectional terminal area was measured per cell and then normalized to the respective BC cross-sectional area. Animals with hearing loss showed greater variability, and terminals were smallest for 6-month-old *sh2*$^{-/-}$ mice. **(B)** Total unlabeled terminal apposition was measured per cell and then taken as a percentage of the respective BC cross-sectional perimeter. A reduction in relative apposition length was seen in older *sh2*$^{-/-}$ mice. **(C)** Total mitochondrial fraction of all unlabeled terminals per BC. Data points for all graphs represent individual cell measures. Bars indicate mean ± SD. Different symbols indicate samples from different subjects. † denotes significant within-cohort variability. *$p \leq 0.05$; **$p \leq 0.01$; ***$p \leq 0.001$; ****$p \leq 0.0001$.

Figure 11. Postsynaptic density profiles from unlabeled terminals. PSDs from unlabeled terminals were identified as a dark thickening of the postsynaptic membrane apposing presynaptic clustering of synaptic vesicles. The limits of the PSDs are demarcated by arrowheads. PSD profile length and curvature varied in all animal cohorts, irrespective of hearing status. However, the majority of PSDs were concave with respect to the terminal, and expressed an asymmetric PSD, both characteristics of AN terminals. Examples are shown from 6-month-old CBA/Ca (A-B), DBA/2 (C-D), and *sh2*$^{-/-}$ (E-F) mice.

Figure 12. Postsynaptic density profile apposition, length, and curvature from unlabeled terminals. (A) Total PSD profile apposition was measured per cell and then taken as a percentage of the respective BC cross-sectional perimeter. There was no trend in PSD apposition with hearing status. **(B)** Lengths of individual PSD profiles were highly variable and relatively similar across cohorts. **(C)** Positive curvature values indicate concave PSDs relative to the terminal, negative values indicate convex PSDs, and a value of 0 indicates a flat PSD. The majority of PSDs were concave, characteristic of AN terminals. Results suggest a slight flattening of PSDs with hearing loss. Bars indicate mean ± SD. Different symbols indicate samples from different subjects. † denotes significant within-cohort variability. **$p \leq 0.01$; ***$p \leq 0.001$; ****$p \leq 0.0001$.

Table 1. Cochlear Nucleus Reconstructions and Alignment to Template

Mouse		Cochlear Nucleus Alignment					
		VCN Volume			VCN Width		
Strain	Age (mo.)	Pre-Align (mm^3)	Post-Align (mm^3)	Change (%)	Pre-Align (μm)	Post-Align (μm)	RMS Error (μm)
CBA/Ca	1	0.275	0.308	12%	197.0	204.6	36.1
CBA/Ca	1	0.259	0.313	21%	192.8	205.4	36.6
CBA/Ca	3	0.349	0.298	-14%	213.6	203.1	40.6
CBA/Ca	3	0.326	0.300	-8%	200.4	194.9	39.9
CBA/Ca	6	0.333	0.296	-11%	199.1	191.5	36.8
CBA/Ca	6	0.279	0.286	2%	175.6	176.7	46.7
CBA/Ca	6	0.354	0.303	-15%	207.9	197.0	36.0
CBA/Ca	6	0.342	0.311	-9%	200.2	194.0	36.4
sh2$^{+/-}$	1	0.316	0.297	-6%	193.9	189.9	44.2
sh2$^{+/-}$	3	0.347	0.307	-11%	194.9	187.4	43.9
sh2$^{+/-}$	6	0.310	0.266	-14%	194.3	184.8	50.3
sh2$^{+/-}$	6	0.285	0.317	12%	194.7	202.2	44.6
DBA/2	1	0.239	0.309	29%	184.7	201.1	42.8
DBA/2	1	0.218	0.296	36%	171.8	190.3	40.0
DBA/2	3	0.276	0.288	4%	185.5	187.9	45.0
DBA/2	3	0.215	0.274	27%	153.4	166.1	52.5
DBA/2	3	0.236	0.293	24%	165.3	177.6	47.6
DBA/2	6	0.293	0.257	-12%	165.1	158.2	60.3
DBA/2	6	0.234	0.272	16%	152.9	160.6	53.1
sh2$^{-/-}$	1	0.266	0.259	-3%	177.4	175.6	57.0
sh2$^{-/-}$	1	0.241	0.320	33%	177.6	195.3	43.2
sh2$^{-/-}$	3	0.262	0.250	-5%	168.4	165.5	59.1
sh2$^{-/-}$	3	0.276	0.289	5%	171.2	174.0	45.5
sh2$^{-/-}$	3	0.295	0.298	1%	168.1	168.7	51.5
sh2$^{-/-}$	6	0.326	0.290	-11%	197.1	189.6	47.4
sh2$^{-/-}$	6	0.261	0.247	-5%	184.5	181.3	52.7

Table 2. Light Microscopy Results

Mouse			Bushy Cells		Endbulbs of Held		
Strain	Age (mo.)	N	Area (μm^2)**	n	Silhouette Area (μm^2)**	Shape Factor**	n
CBA/Ca	1	2	205.4 ± 32.2	39	71.51 ± 18.27	20.21 ± 2.90	40
CBA/Ca	3	3*	205.5 ± 18.3	46	71.62 ± 16.77	23.22 ± 3.35	23
CBA/Ca	6	4	214.5 ± 24.3	45	61.69 ± 24.08	18.07 ± 4.14	31
sh2$^{+/-}$	1	2*	216.1 ± 30.3	34	71.85 ± 16.40	20.78 ± 4.61	33
sh2$^{+/-}$	3	3*	201.3 ± 25.6	67	78.61 ± 15.03	20.10 ± 3.05	49
sh2$^{+/-}$	6	2	209.8 ± 32.1	62	62.76 ± 26.24	19.40 ± 4.00	43
DBA/2	1	2	212.5 ± 19.1	26	75.67 ± 22.65	20.27 ± 3.41	25
DBA/2	3	3	188.4 ± 26.6	58	59.95 ± 25.45	25.28 ± 5.11	51
DBA/2	6	2	183.4 ± 27.7	66	43.36 ± 16.92	21.42 ± 5.59	31
sh2$^{-/-}$	1	2	201.3 ± 25.0	48	66.33 ± 21.80	19.31 ± 4.36	41
sh2$^{-/-}$	3	3	179.4 ± 16.0	37	40.22 ± 16.82	17.95 ± 3.29	39
sh2$^{-/-}$	6	4*	171.7 ± 24.1	68	36.89 ± 16.69	13.50 ± 3.04	28

**Additional cases included that were not reconstructed in 3D.*

***See Figures 4 and 7 for statistical comparisons.*

Table 3. Summary of Subjects for Ultrastructure Analyses

Mouse		Histology			Postsynaptic Densities		
Strain	Age (mo.)	N	Perfusion Solution*	Antibody Stain	BC n	# PSDs per BC	Curvature (μm^{-1})
CBGlyT2	3	1 2	4%P 2%P/2%G	GFP	26	8.27 ± 4.3	1.88 ± 2.51
CBGlyT2	6	1 2	4%P 2%P/2%G	GFP	25	9.38 ± 3.3	1.71 ± 1.95
sh2$^{+/-}$GlyT2	3	2 1	4%P 2%P/2%G	GFP	22	8 ± 3.7	1.97 ± 2.55
sh2$^{+/-}$GlyT2	6	3	4%P	GFP	24	8.96 ± 3	2.49 ± 2.62
DBA/2	3	3	4%P	GlyT2	37	10.42 ± 3.8	1.50 ± 2.20
DBA/2	6	3	4%P	GlyT2	24	8.8 ± 4	1.26 ± 2.14
sh2$^{-/-}$GlyT2	3	3	2%P/2%G	GFP	33	9.91 ± 3.2	1.55 ± 2.41
sh2$^{-/-}$GlyT2	6	2 1	4%P 2%P/2%G	GFP	30	9.59 ± 5.7	1.36 ± 2.23

**G, glutaraldehyde; P, paraformaldehyde*

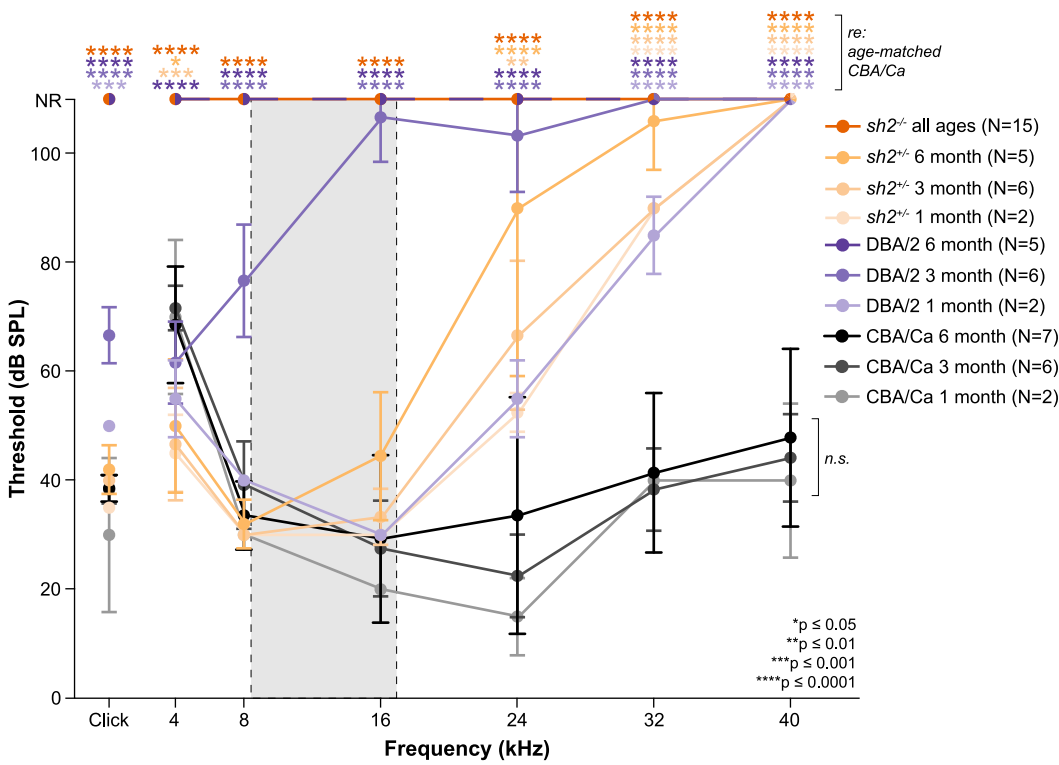
re:
age-matched
CBA/Ca
NR
100
80
60
40
20
0
Threshold (dB SPL)
sh2-/- all ages (N=15)
sh2+/- 6 month (N=5)
sh2+/- 3 month (N=6)
sh2+/- 1 month (N=2)
DBA/2 6 month (N=5)
DBA/2 3 month (N=6)
DBA/2 1 month (N=2)
CBA/Ca 6 month (N=7)
CBA/Ca 3 month (N=6)
CBA/Ca 1 month (N=2)
n.s.
*p ≤ 0.05
**p ≤ 0.01
***p ≤ 0.001
****p ≤ 0.0001
Click
4
8
16
24
32
40
Frequency (kHz)

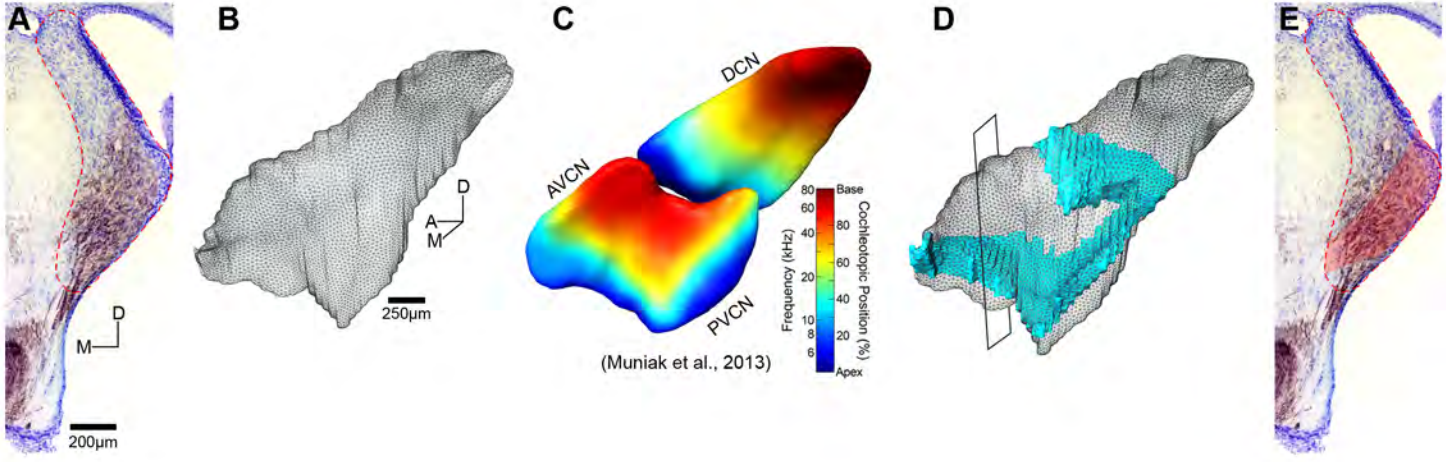
A
D
M
200µm
B
D
A
M
250µm
C
DCN
AVCN
PVCN
(Muniak et al., 2013)
Frequency (kHz)
80
60
40
20
10
8
6
Base
80
60
40
20
Apex
Cochleotopic Position (%)
D
E

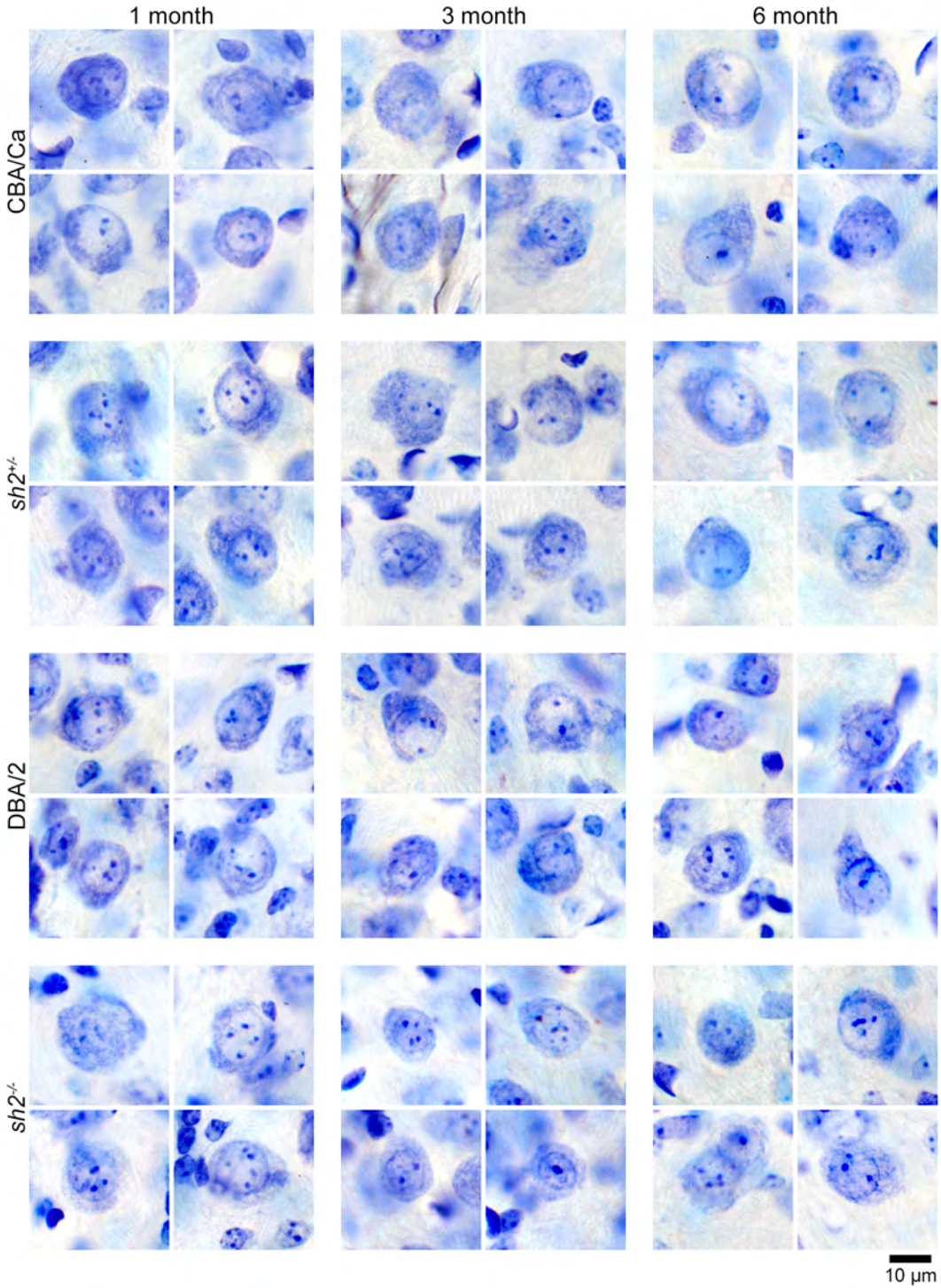
1 month
3 month
6 month
CBA/Ca
sh2+/-
DBA/2
sh2-/-
10 µm

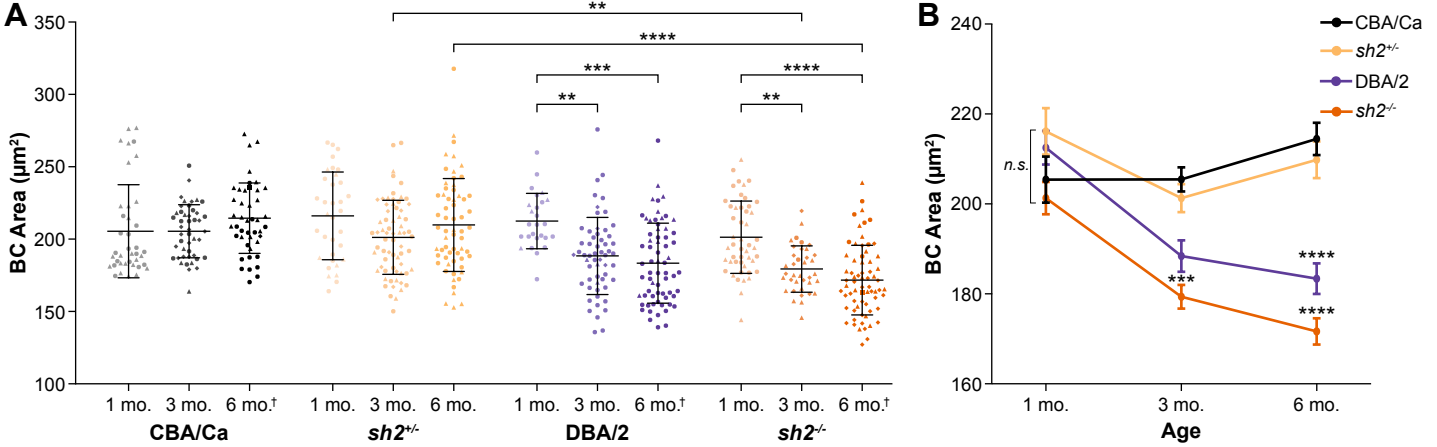
A
BC Area (µm²)
350
300
250
200
150
100
**
****
***
**
**
****
1 mo.
3 mo.
6 mo.†
1 mo.
3 mo.
6 mo.
1 mo.
3 mo.
6 mo.†
1 mo.
3 mo.
6 mo.†
CBA/Ca
sh2+/-
DBA/2
sh2-/-
B
BC Area (µm²)
240
220
200
180
160
CBA/Ca
sh2+/-
DBA/2
sh2-/-
n.s.
***
****
****
1 mo.
3 mo.
6 mo.
Age

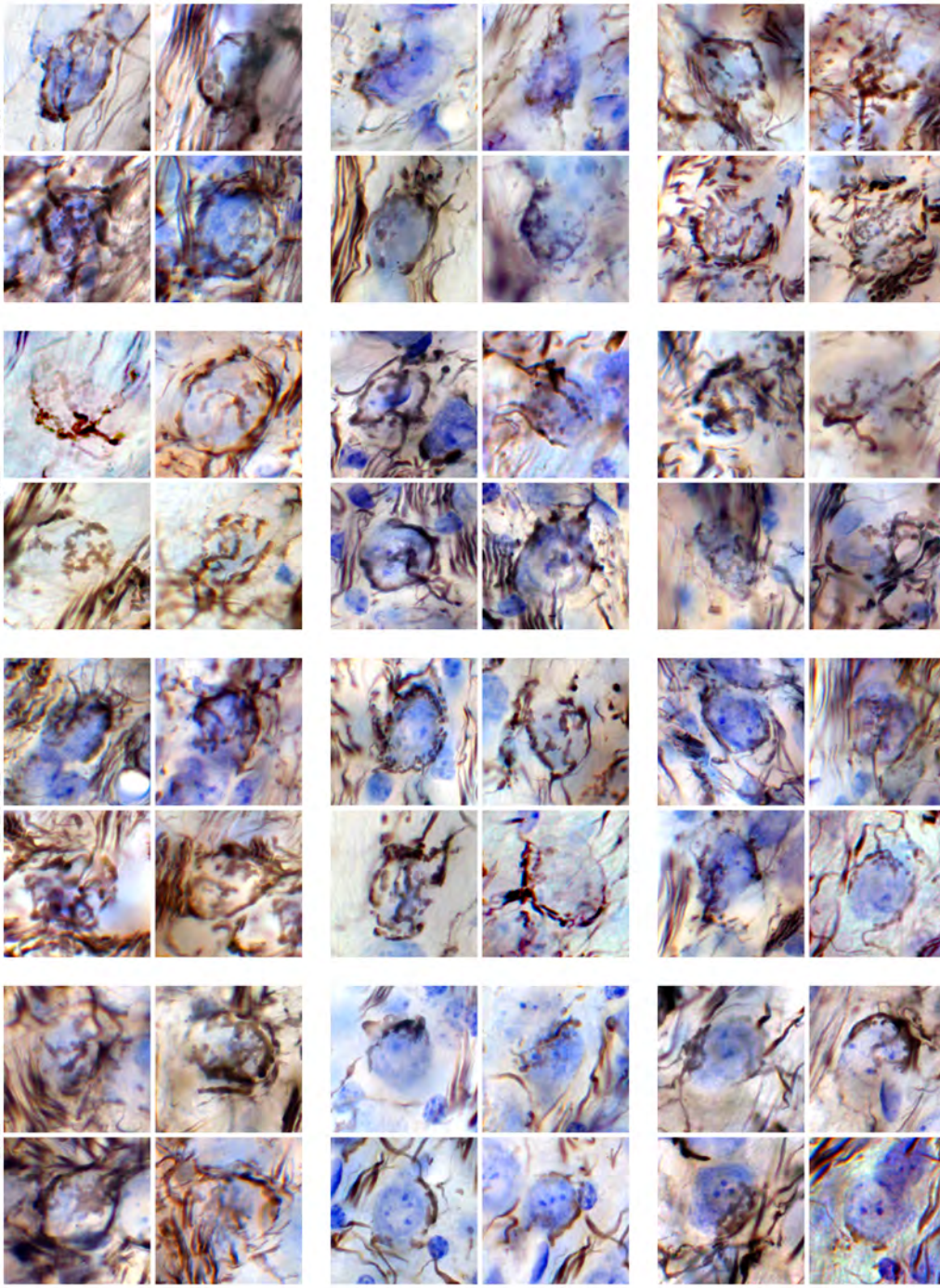
1 month
3 month
6 month
CBA/Ca
sh2+/-
DBA/2
sh2-/-
10 µm

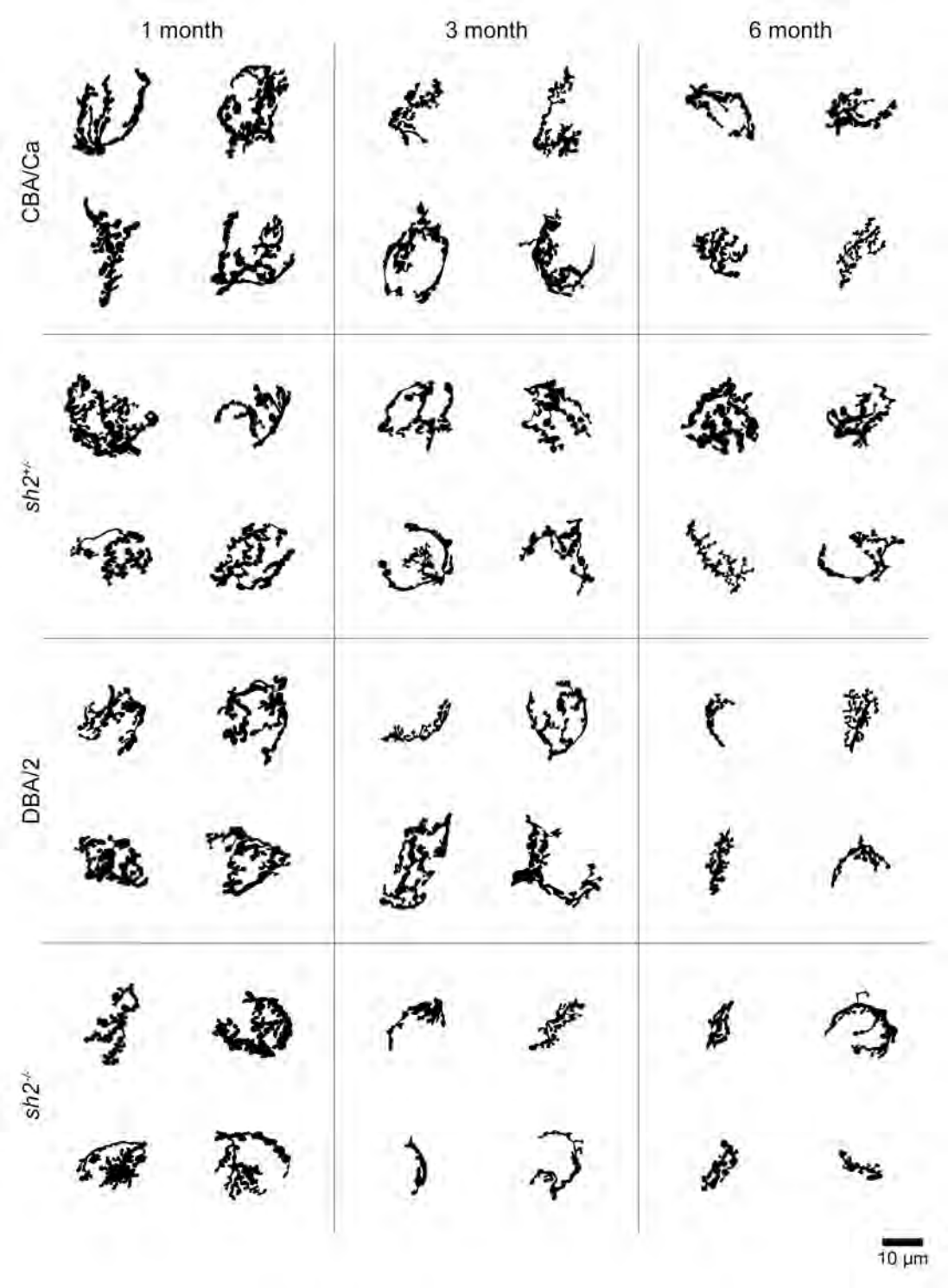
1 month
3 month
6 month
CBA/Ca
sh2+/-
DBA/2
sh2-/-
10 µm

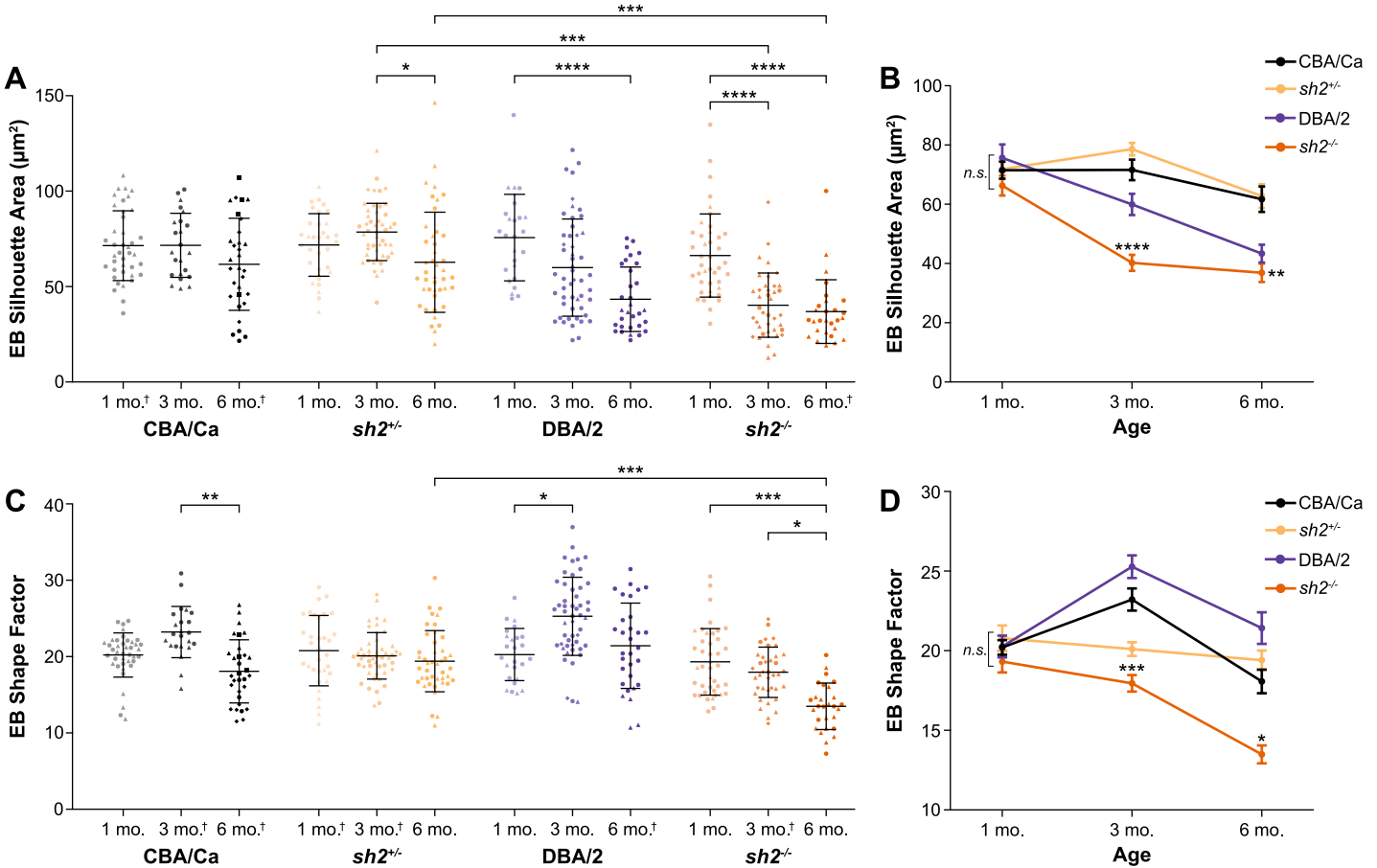
A
EB Silhouette Area (µm²)
150
100
50
0
***
***
*
****
****
****
1 mo.† 3 mo. 6 mo.†
CBA/Ca
1 mo. 3 mo. 6 mo.
sh2+/-
1 mo. 3 mo. 6 mo.
DBA/2
1 mo. 3 mo. 6 mo.†
sh2-/-
B
EB Silhouette Area (µm²)
100
80
60
40
20
0
n.s.
****
**
1 mo. 3 mo. 6 mo.
Age
CBA/Ca
sh2+/-
DBA/2
sh2-/-
C
EB Shape Factor
40
30
20
10
0
**
***
*
***
1 mo. 3 mo.† 6 mo.†
CBA/Ca
1 mo.† 3 mo.† 6 mo.
sh2+/-
1 mo. 3 mo. 6 mo.†
DBA/2
1 mo. 3 mo.† 6 mo.
sh2-/-
D
EB Shape Factor
30
25
20
15
10
n.s.
***
*
1 mo. 3 mo. 6 mo.
Age
CBA/Ca
sh2+/-
DBA/2
sh2-/-

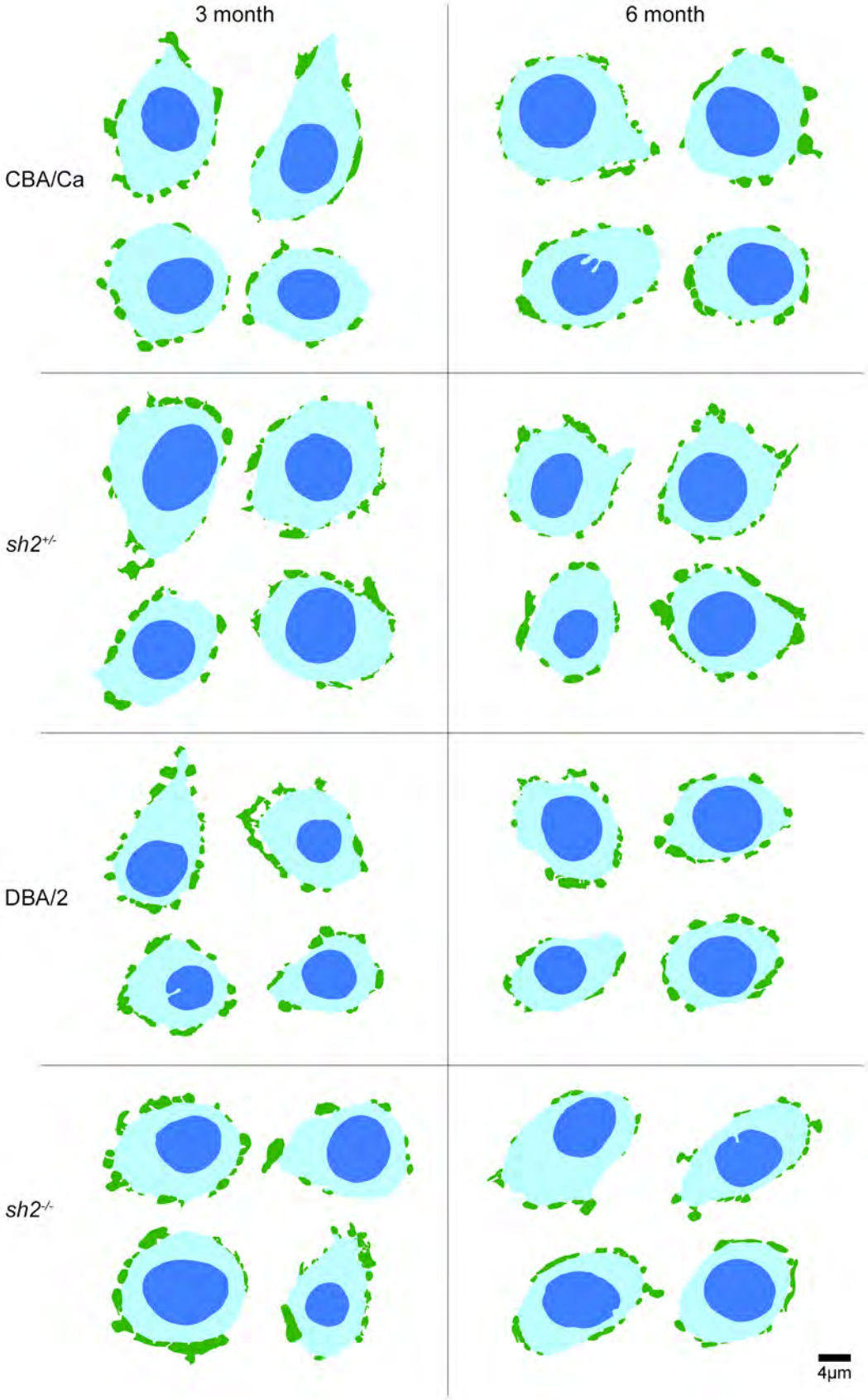
3 month
6 month
CBA/Ca
sh2+/-
DBA/2
sh2-/-
4μm

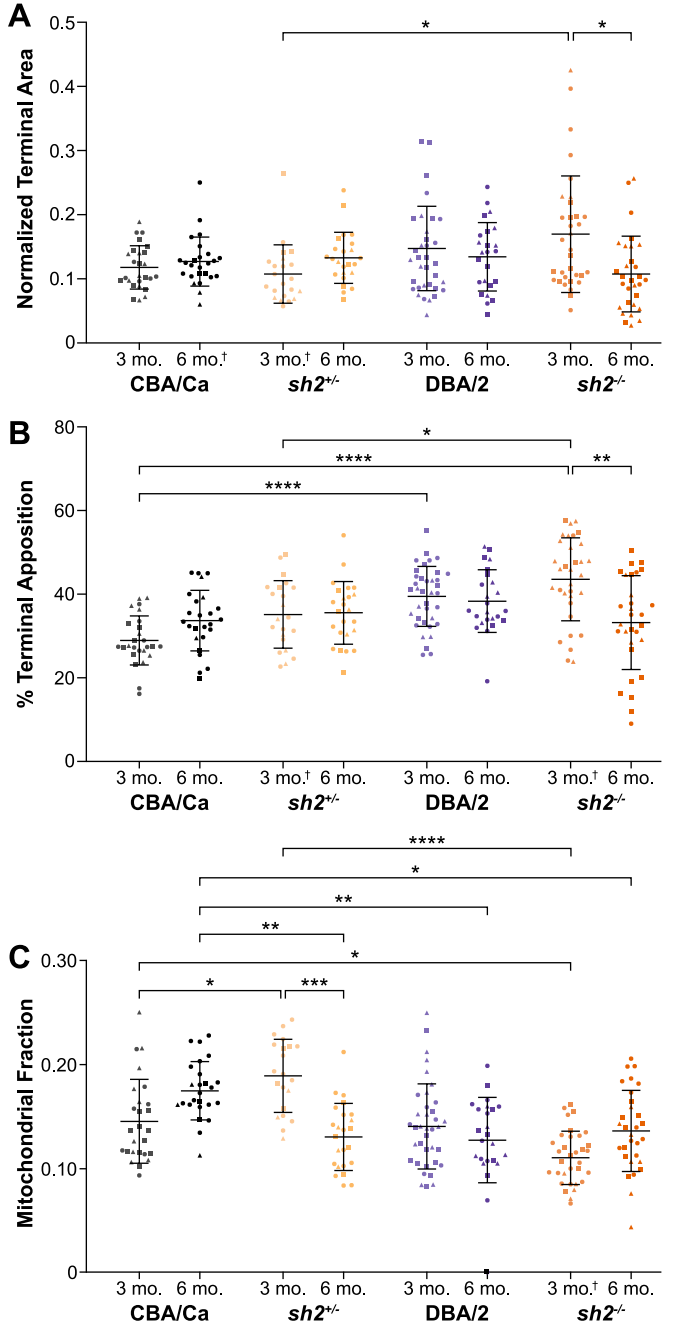
A
Normalized Terminal Area
0.5
0.4
0.3
0.2
0.1
0
*
*
3 mo.
6 mo.†
3 mo.†
6 mo.
3 mo.
6 mo.
3 mo.
6 mo.
CBA/Ca
sh2+/-
DBA/2
sh2-/-
B
% Terminal Apposition
80
60
40
20
0
*
****
**
****
3 mo.
6 mo.
3 mo.†
6 mo.
3 mo.
6 mo.
3 mo.†
6 mo.
CBA/Ca
sh2+/-
DBA/2
sh2-/-
C
Mitochondrial Fraction
0.30
0.20
0.10
0
****
*
**
**
*
*
***
3 mo.
6 mo.
3 mo.
6 mo.
3 mo.
6 mo.
3 mo.†
6 mo.
CBA/Ca
sh2+/-
DBA/2
sh2-/-

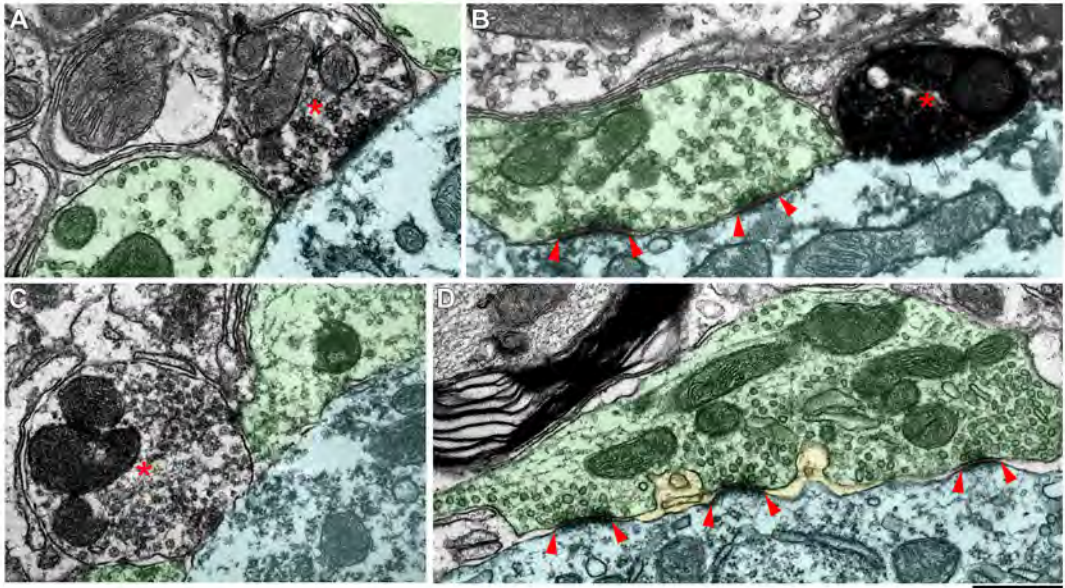
A
B
C
D
500nm

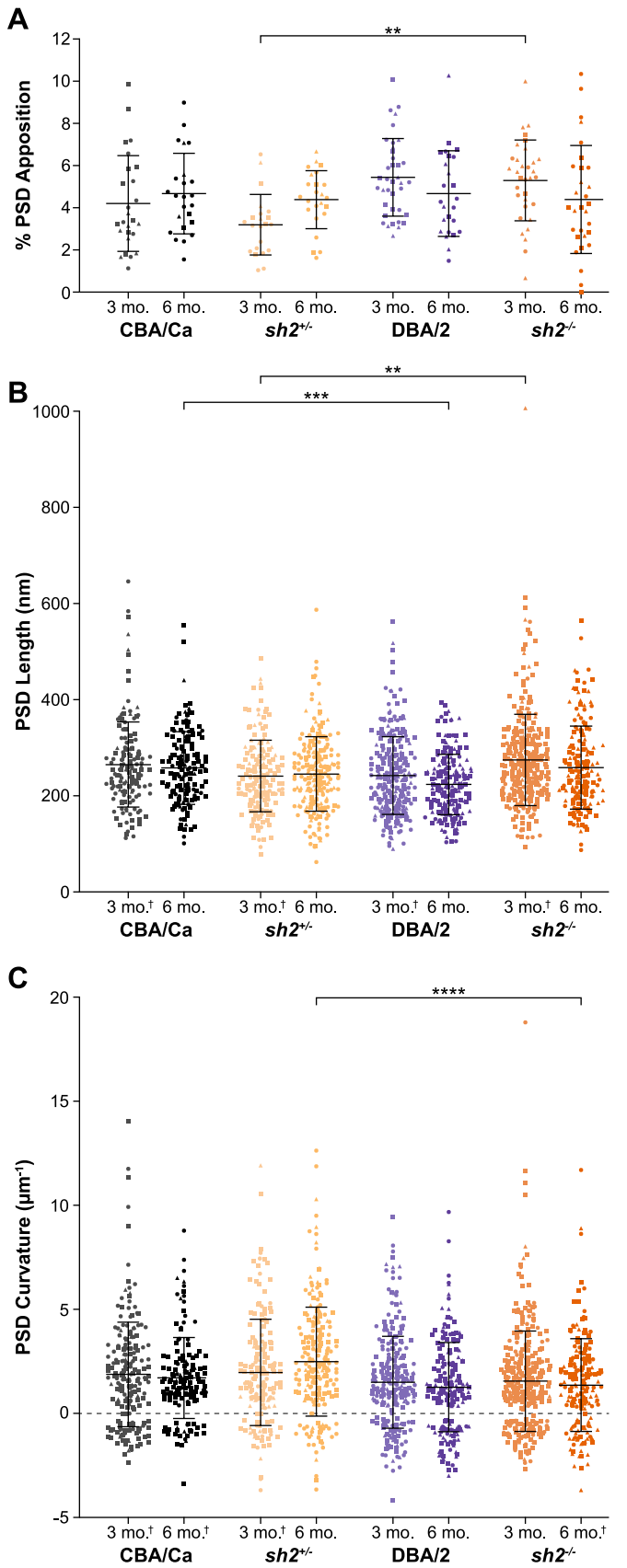
A
% PSD Apposition
12
10
8
6
4
2
0
**
3 mo.
6 mo.
3 mo.
6 mo.
3 mo.
6 mo.
3 mo.
6 mo.
CBA/Ca
sh2+/-
DBA/2
sh2-/-
B
PSD Length (nm)
1000
800
600
400
200
0
**
***
3 mo.†
6 mo.
3 mo.†
6 mo.
3 mo.†
6 mo.
3 mo.†
6 mo.
CBA/Ca
sh2+/-
DBA/2
sh2-/-
C
PSD Curvature (µm-1)
20
15
10
5
0
-5
****
3 mo.†
6 mo.†
3 mo.†
6 mo.
3 mo.
6 mo.
3 mo.
6 mo.†
CBA/Ca
sh2+/-
DBA/2
sh2-/-

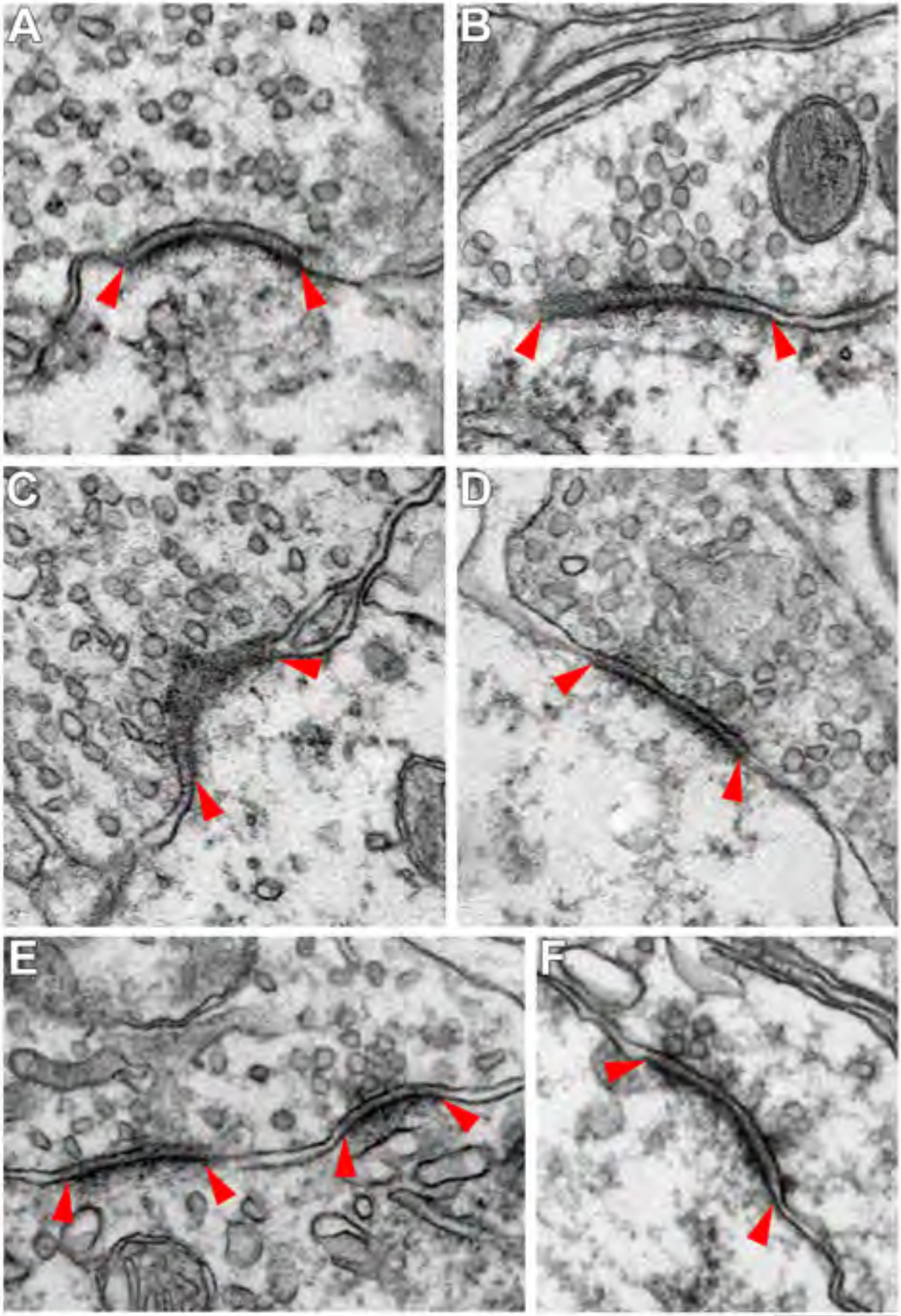
A
B
C
D
E
F
250nm